

Coda Wave Interferometry Analysis for Brittle Rock Deformation during Uniaxial Compression

Thijs Johannes Boerrigter

Thesis Committee:

Dr. A. Barnhoorn - supervisor

Ir. R. Zotz-Wilson - daily supervisor

Dr. Ir. G.G. Drijkoningen

Prof. Dr. P.J.L. Zitha

MSc thesis

June 29, 2017



Coda Wave Interferometry Analysis for Brittle Rock Deformation during Uniaxial Compression

by

Thijs Johannes Boerrigter

to obtain the degree of

Master of Science

In Petroleum Engineering and Geosciences

at the Delft University of Technology,
to be defended publicly on Thursday June 29, 2017 at 12:00 PM.

Student number:	4017862	
Thesis committee:	Dr. A. Barnhoorn,	TU Delft, supervisor
	Ir. R. Zotz-Wilson,	TU Delft, daily supervisor
	Dr. Ir. G.G. Drijkoningen,	TU Delft
	Prof. Dr. P.J.L. Zitha,	TU Delft

An electronic version of this thesis is available at <http://repository.tudelft.nl/>.

Abstract

Coda Wave Interferometry analysis is studied for rocks subjected to brittle deformation which is induced by an Uniaxial Compressive Strength testing machine. Ultrasonic pulses, 1 MHz and 2.25 MHz, are sent through rock samples and recorded throughout the loading up-to failure. A novel method is proposed, the rolling cross correlation, which can aid in the identification of the brittle fracture process. Unlike in previous CWI research a different method of referencing is used. The focus is not on velocity change of the medium with a fixed reference wavelet, but a variable reference point is used with a lag in respect to the newly measured wavelet. With this rate-of change method it is possible to quantify an incremental change in the scatter distribution as a result of micro-fracturing. Laboratory testing results showed similar curve behavior for the following rock types: Bentheimer Sandstone, Fontainebleau Sandstone, Indiana limestone and the Benin Granite. A correlation was found between the rolling cross correlation curves and the geomechanical phases of initial crack closure, purely elastic region and inelastic deformation. The detection of the latter was found to be a precursory indicator for yielding and eventually rock failure. The trend of the rolling cross correlation curve became more erratic when using a higher frequency as pulse source. In some cases individual events of faster displacement rate due to fracturing were detected in the change of coda waves. CWI analysis identified as an interesting tool for monitoring in-situ rock, such as fault stability in earthquake prediction, though future research is needed to enhance the correlation of change in coda to the actual change in the medium.

Contents

1	Introduction	1
2	Theory	3
2.1	Rock Mechanics	3
2.1.1	Loading stages, stress-strain diagram	3
2.2	Acoustics	4
2.2.1	Coda part of wavelet	4
2.2.2	Coda Wave Interferometry	5
3	Experimental set-up	7
3.1	Unconfined Compressive Strength test and acoustic setup	7
3.2	Rock types tested	9
3.2.1	Bentheim sandstone	9
3.2.2	Fontainebleau sandstone	9
3.2.3	Indiana limestone	10
3.2.4	Benin granite	10
4	Geomechanics	13
4.1	Stress-strain results	13
4.2	Discussion	14
5	CWI	17
5.1	CWI results	17
5.1.1	Reference points in cross-correlation	17
5.1.2	Location of receivers	19
5.1.3	Correlation lag	20
5.1.4	Correlation window sizes and positions	21
5.1.5	CWI with stress-strain curves	23
5.1.6	Bentheim Sample	23
5.1.7	Other rocktypes	23
5.1.8	Change in source frequency	26
5.1.9	General results overview	29
5.2	Discussion CWI	31
5.2.1	Cross Correlation Coefficient	31
5.2.2	Acoustic scattering phases	32
5.2.3	Linking of the geomechanical phases with the acoustic phases	38
5.2.4	Frequency and microfracture size	38
5.3	Comparison with AE monitoring and use in Earthquake prediction.	40
6	Conclusion	43
	Acknowledgements	45
	Bibliography	47
	Appendices	49
	A	51
	B	53
	C	55



Introduction

Understanding and quantifying the behavior of micro-fracturing in rocks under pressure which may lead to major cracking or failure is important for various applications, such as: earthquake prediction (fault zone stability) [25], hydraulic fracturing [19], borehole breakout prevention (avoiding sand production)[11],reservoir monitoring, nuclear fuel waste storage [13] and other rock stability monitoring scenarios. The microfracturing process is of interest also for other materials which show brittle deformation, for example concrete failure in civil engineering structures [36].

Research on behavior and/or irregularities in rocks often make use of seismic waves. The non-destructive character of this elastic wave propagation and the possibility of testing in-situ makes ultrasonic analysis an interesting field of research for flaw and crack detection, especially with the smaller wavelengths of ultrasonic frequencies (frequencies above audible sound, >20 kHz). Various methods making use of ultrasonic analysis have been studied extensively and applied with varying success, for instance: Ultrasonic Pulse Velocity (UPV), Q-factor (change in pulse shape) and Acoustic Emission (AE) [4].

In this study a different method will be applied to ultrasonic pulse data, namely Coda Wave Interferometry (CWI) analysis. Similar to UPV analysis this is an active technique, where an ultrasonic pulse is shot and recorded but contrary to UPV the focus is on the later arrivals. The theory uses the principal that the later arrivals have had a longer propagation path, thus are more sensitive to the changes in the medium [39]. The CWI analysis is done with laboratory tests, by uniaxial loading a rock to failure while multiple waves are recorded with a fixed time interval throughout the experiment. Previous research with similar methodology but different data processing methods showed that the wave velocity only decreases marginally when traveling through fractured rock, but that attenuation is more sensitive to fractures and that a minimum in attenuation was found before the first fracturing occurred [1][42][15]. As far as known, pressurization of a rock in controlled laboratory conditions while monitoring the coda waves has only been done by A. Grêt, R. Snieder and J. Scales [17]. In their research the emphasis was on the stress difference and not on the brittle deformation itself, where they found strong correlation between wavelets but with a velocity change due to the stress differences.

To the best of my knowledge no research of CWI applied to brittle rock deformation itself was available. The main focus in this research was to study general coda-wave behavior of rocks brought to failure and not the specific behavior of a single rock type. The rock types vary from typical reservoir rocks with different geomechanical properties and/or mineral content to a crystalline rock. The rock types tested are: Bentheimer Sandstone, Fontainebleau Sandstone, Indiana Limestone (carbonate) and the Benin Granite.

2

Theory

2.1. Rock Mechanics

2.1.1. Loading stages, stress-strain diagram

In this thesis an attempt will be made to link the rock fracture process to CWI analysis. The most used and clear tool for fracture analysis will be used, namely stress-strain curves. The rock samples are deformed in a displacement controlled test, purely subjected to axial stress. Brace and Bieniawski used similar testing procedures and showed with laboratory studies that the deformation of a rock can be described in five stages until rupture [3] [7]. A schematic example of a stress-strain curve with the corresponding stages is shown in Figure 2.1.

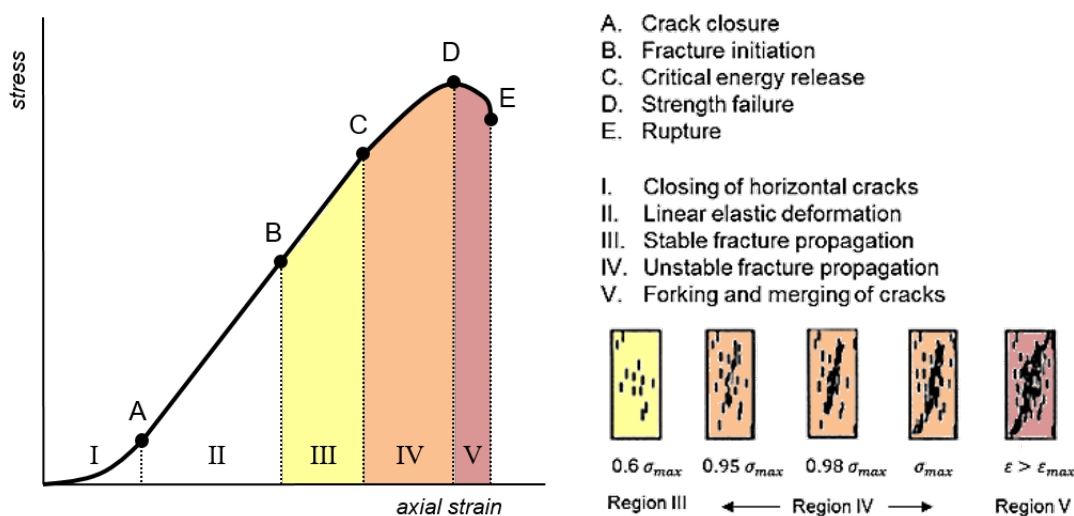


Figure 2.1: At the left the different stages of loading are shown in terms of stress-strain as described by Brace and Bieniawski. At the right the forming of microcracks in the different stages is shown as described by Hallbauer.(modified after Hallbauer and Bieniaswki)[20][3]

Each of these stages is bounded by a threshold corresponding to the main occurring process indicated with the letters A,B,C,D and E. During the first phase, crack closure, pre-existing fractures orientated normal to the axial stress will close. The resulting accumulated strain does not behave linear with stress in this stage. When most cracks are closed the elastic stage will follow, where in theory the accumulated strain is purely linear. The first stable microfractures are formed in the third stage. Hallbauer et al. observed the changes during each stage microscopically and found that in stage three the first microcracks were formed. In Figure

2.1 at the right, schematics are shown of the formation of microfractures in the stages of permanent deformation, stage III to stage V [20]. The theory of formation and growth of these microfractures is an elaboration of Griffith's theory, where microcracks are formed due to high stress concentrations when an energy activation threshold is reached at so called flaws in the rock, such as: voids, inclusions or grain contacts [34] [24] [18]. An increase in microfracturing occurs in stage four. At this point the formed cracks consists of predominantly unstable cracks. An unstable crack does not immediately stop growing after the stress is released [3], which will result in non-linear behavior because less stress is needed for the same proportional increase in strain. The transition of predominantly stable crack growth to predominantly unstable crack growth is often referred to as the yield stress or yield point [3] [29]. This term is not always used consistently in literature, instead it is sometimes referred to as the point where the first microfractures are formed [14] [32]. However, there is general consensus that the yield point is the sudden change of slope from linear to nonlinear behavior [23] [29] [32], which occurs, after the first unstable micro-cracks have formed as can be seen in 2.1. The final stage consists of merging the microfractures until rupture occurs and the integrity of the rock is lost. The main failure mechanisms in brittle deformation are shear fractures or tensile fractures [32].

2.2. Acoustics

2.2.1. Coda part of wavelet

An acoustic wave sent into a rock medium will be received altered with respect to the source wave. One reason for higher attenuation is an increase of multiple scattering, which will result in a higher energy loss of the initial source pulse [27] [44]. The received wavelet consist of multiple wave modes, such as: first arrivals, multiple arrivals, surface waves, random interface bouncing and multiple scattered waves [16]. A schematic of the different paths travelled per wavemode is shown in Figure 2.2

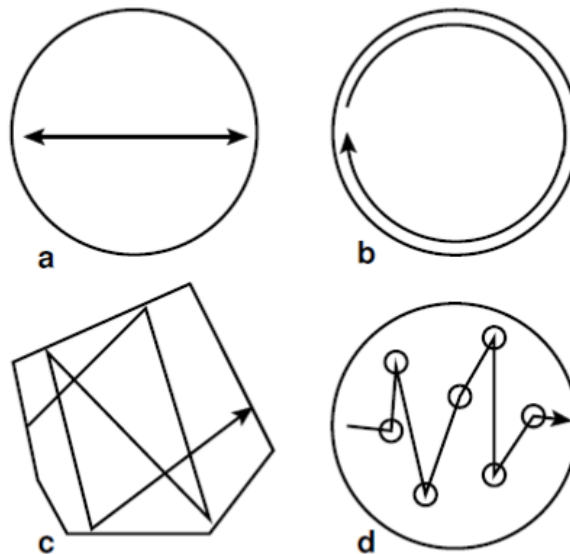


Figure 2.2: Wavemode travel paths. a. Direct and multiple arrivals between starting point and end point. b. Surface wave along the boundaries of the medium. c. Multiple interface bouncing, reverberations. d. Multiple scattering due to scatters in the medium. [16]

The portion of the wavefield focused on in this thesis are the waves deformed due to multiple scattering, referred to as the coda part or diffuse field. In theory pure coda consists of incoherent waves scattered due to randomly distributed heterogeneity in the medium [35]. In Figure 2.3 an example is shown from a received wavelet transmitted through a sandstone, originating from a p-wave pulse as the source. Here the coda is the part of the wavelet arriving directly after the early arrivals [17]. A clear distinction of the wavelet is difficult, due to the multiple wave modes arriving simultaneously.

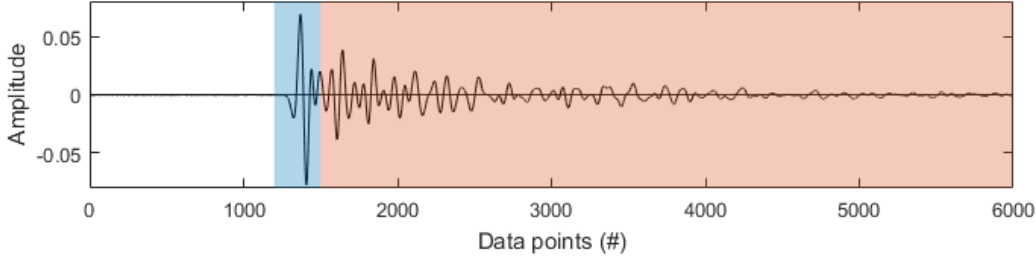


Figure 2.3: Wavelet with First Arrival indicated with blue and coda with red.

The coda has long been neglected, but the high reproducibility of the coda part makes it interesting to detect changes in a medium [40].

2.2.2. Coda Wave Interferometry

Coda Wave Interferometry (CWI) is a method proposed by Roel Snieder by which the similarity of the coda part of a wave can be used to assess changes in a medium [40]. To assign a value for similarity between two waves a normalized time-shifted Cross-correlation Coefficient (CC) is used:

$$R^{(t,t_w)}(t_s) = \frac{\int_{t-t_w}^{t+t_w} u_{unp}(t') u_{per}(t' + t_s) dt'}{\left(\int_{t-t_w}^{t+t_w} u_{unp}^2(t') dt' \int_{t-t_w}^{t+t_w} u_{per}^2(t' + t_s) dt' \right)^{\frac{1}{2}}} \quad (2.1)$$

An unperturbed signal $u_{(unp)}$, fixed reference point, is compared with a perturbed signal $u_{(per)}$ at time t' where a velocity change of magnitude t_s has occurred. As we search for the largest R for many different t_s we in the end find the actual velocity change of the two wavefields. Only a specific part of the signal is cross-correlated, indicated by a window with center t and a window length of $2t_w$. An important assumption in Equation 2.1 is that the perturbation of the scatterers are much smaller than the mean free path the elastic wave has traveled [40] [17]. These are existing scatterers and not newly formed in the medium. Various research has that CWI is able to monitor subtle perturbations in a mediums velocity [17] [37].

This research aims to monitor a different type of process; the permanent change of the amount and distribution of scatterers in a medium caused by compressing a rock to failure. A new method is proposed to better identify the behavior corresponding to this ongoing process of incremental change. This is done by enforcing the reference point to move along with the signal it is compared to, such that a correlation coefficient over a certain measurement interval is obtained and not a comparison with a fixed reference point as shown in Figure 2.4. From now on this method will be referred to as the Rolling Cross-correlation Coefficient (RCC). The equation for the RCC is obtained by rewriting Equation 2.1 to:

$$R^{(n,L)(t,t_w)}(t_s) = \frac{\int_{t-t_w}^{t+t_w} u_n(t') u_{n+L}(t' + t_s) dt'}{\left(\int_{t-t_w}^{t+t_w} u_n^2(t') dt' \int_{t-t_w}^{t+t_w} u_{n+L}^2(t' + t_s) dt' \right)^{\frac{1}{2}}} \quad (2.2)$$

$$\text{For } n = 1, 2, \dots, (N - L)$$

This equation is similar with Equation 2.1 except that there are two new variables: n and L . Number n is the position of the reference measurement to which the measurement with a positive correlation lag difference (L) is compared to. (The last measurement taken is measurement N .) These new variables, n and L , must be selected for the data processing itself, but the generated outcome is not trivial. Variation of these variables will be discussed in detail in this thesis.

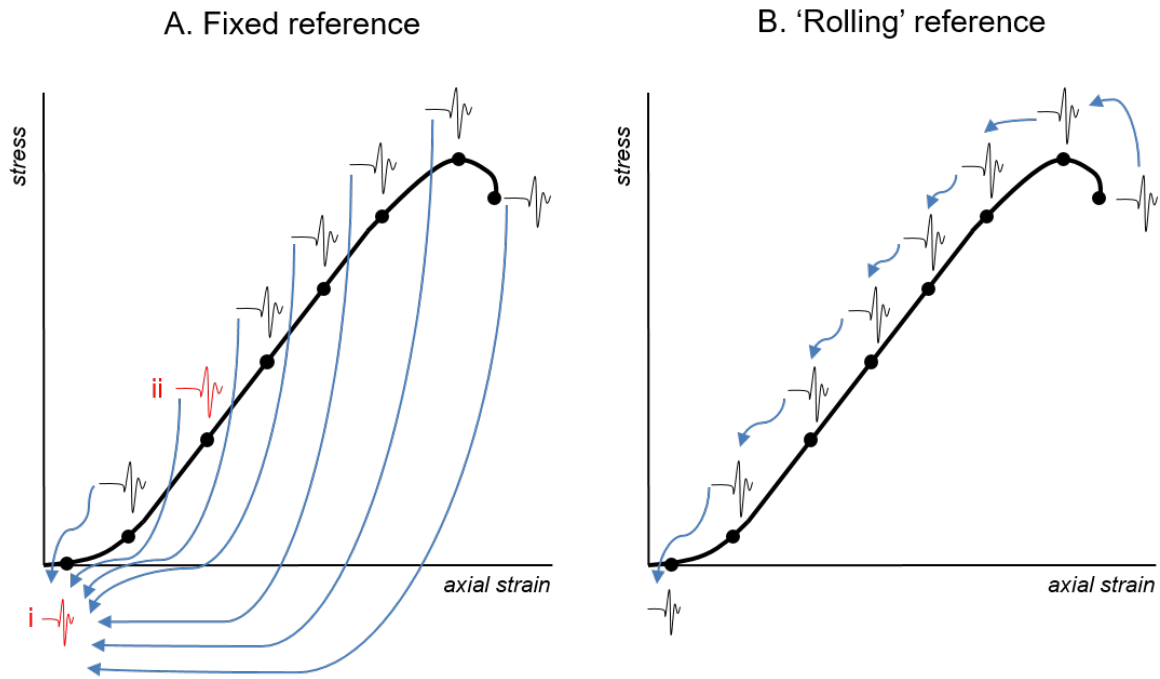


Figure 2.4: The different use of reference point by which each wavelet is correlated shown schematically, where the wavelet which is compared to is indicated with blue arrows. For clarity only 8 points are shown where an acoustic measurement (wavelet) is recorded, while in practice 65 to 400 wavelets were obtained from initial loading to failure. A. With the fixed reference each wavelet is compared with the same wavelet, for instance with the first measurement as shown in this figure (indicated with i) or with a wavelet in the elastic region (indicated with ii). b. With the Rolling Cross-Correlation, each wavelet is compared with its predecessor or with a specified number of wavelets before depending on the correlation lag size (in this case, correlation lag is one measurement).

3

Experimental set-up

3.1. Unconfined Compressive Strength test and acoustic setup

The stress-strain data was gathered with an displacement controlled Unconfined Compressive Strength test (UCS test). The deformation rate varied per rock, but was kept in the same order of magnitude: 0.00005 - 0.0005 mm/s. This rate was chosen dependant on the total strain deformation until failure of the rock, to ensure enough acoustic measurements are taken for CWI analysis. To obtain a well distributed stress distribution with no peak stress in the rock sample Paterson and Wong showed that a ratio between length and diameter must be used of at least 2.5 to 1. As shown in the graph left of Figure 3.1 at this diameter the UCS stays fairly constant, with a stress distribution as shown on the right.

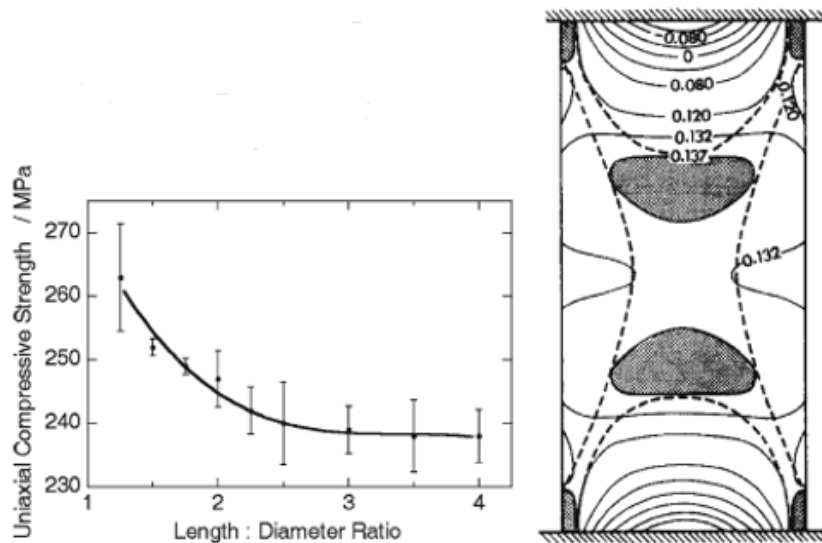


Figure 3.1: The left figure shows the behavior of samples at different Length/diameter ratio's. At approximately the ratio of 2.5 the curve stabilizes and stays constant. At the right the stress distribution is shown when this is fully developed in a sample. (Paterson and Wong)[32]

To be certain there was enough space for the cups with the transducers, a sample length of approximately 75 mm with a diameter of 30 mm was used. With the sample length and the displacement (measured with LDVT's), the strain rate can be calculated as $\epsilon_{axial} = \frac{\Delta L}{L_{initial}}$. In Figure 3.2 the setup is shown. An ultrasonic pulse (p-wave) is first amplified before it is emitted from the source transducer in the axial placed steel cup and its transmitted signal is received by three receiver transducers. The receiver placed axial is encased in a steel cup while the radial mounted receivers are placed in PEEK cups. A single ultrasonic source pulse is used with a frequency of 1 MHz or 2.25 MHz. To ensure this signal is transmitted along each transition a

coupling gel is used at the boundaries. The received signals (first arrival and tail) are recorded automatically with a fixed time interval while the sample is brought to failure. To reduce random noise, multiple wavelets are shot after each other and stacked for each measurement point (256-1024 traces). For each wavelet and stress-strain measurement a time stamp is recorded to ensure the acoustic data can be time-matched with the geomechanical data.

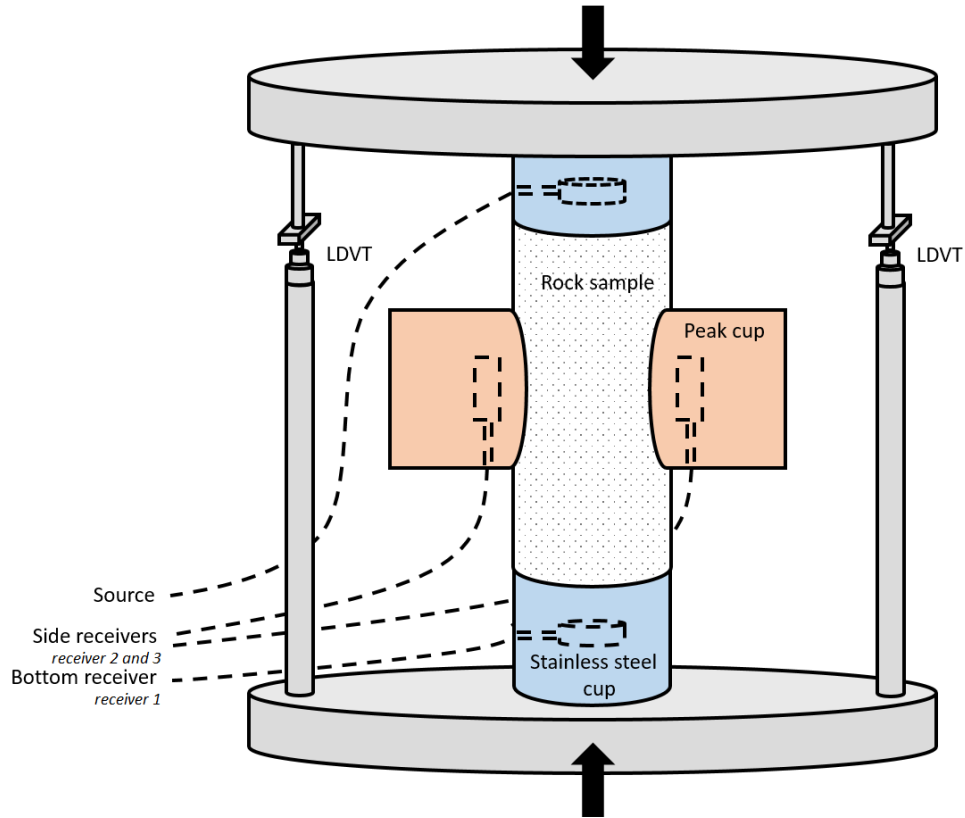


Figure 3.2: Schematic figure of the experimental setup used to gather stress-strain and acoustic data.

3.2. Rock types tested

Four different rock types were tested, namely: Bentheim sandstone, Fontainebleau sandstone, Indiana limestone and a Granite from Benin. The different types of rock were chosen to show the mechanical behavior of the different lithologies. In this section the rocks will be described where possible with the use of literature. No information was available on the Benin granite, so this rock is separately examined microscopically. The different samples are shown in Figure 3.3.

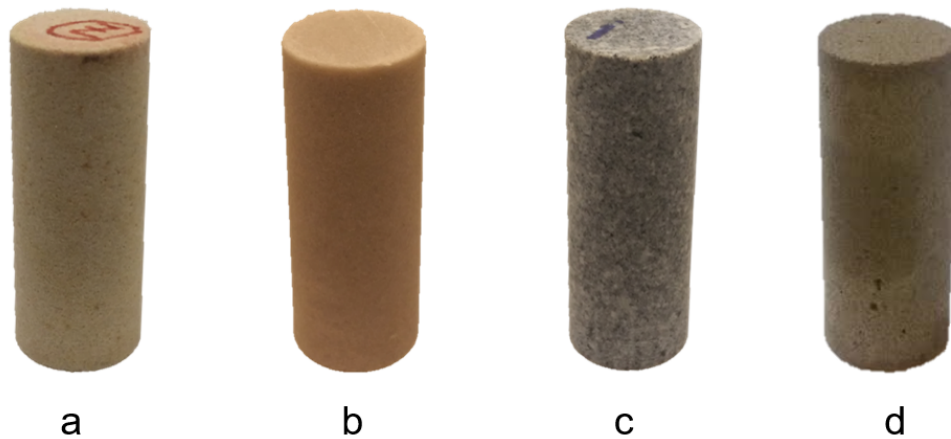


Figure 3.3: Overview of the samples used for this study. From left to right: a. Bentheimer sandstone, b. Fontainebleau sandstone, c. Benin granite, d. Indiana limestone

3.2.1. Bentheim sandstone

The main rock type tested is the Bentheim sandstone. This rock type has been extensively tested and described in literature, making it an ideal rock for experimental testing. Peksa et al.[33] concluded that the Bentheimer sandstone shows lateral consistency, constant mineralogy, block scale homogeneity with a porosity range between 0.21 and 0.27. The well sorted grains consists of the following minerals: quartz (91.7 wt%) , feldspar (4.86 wt%), clay minerals (2.68 wt%), pyrite and iron(hydro)oxides (0.17 wt%). The cementation consists of quartz, originating from overgrowth of the quartz minerals. The grain sizes are in the range from 180 μm and 320 μm . The thinsheet shown in Figure 3.4 provides a visualization description of the rock matrix structure.

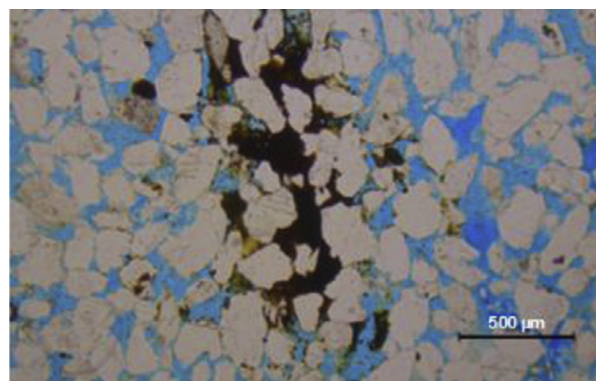


Figure 3.4: Thinsection showing loosely packed Bentheimer sandstone and hematite pore infill. Blue residue was used to show porosity.[33]

3.2.2. Fontainebleau sandstone

The other type of sandstone used is the Fontainebleau sandstone. As for the Bentheim this rock has been experimentally tested and researched intensively, exhibiting well sorted grains slightly smaller in general than the Bentheimer sandstone, with a range between 177 μm and 250 μm . The Fontainebleau sandstone is a pure

quartz rock, where both cement and grains are from quartz.[6][10]. Porosity was found to vary largely in a range of 0.03 and 0.28 [6]. In Figure 3.6 the structure is shown from the research of Cooper et al. [10].

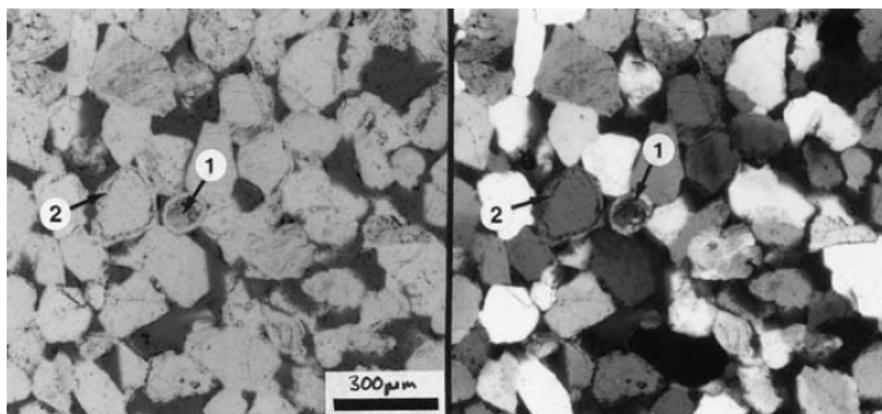


Figure 3.5: Thinsection plane and crossed polarized shown. With numbers 1 and 2 quartz cement overgrowth is indicated. [10]

3.2.3. Indiana limestone

The Indiana limestone is homogeneous and has a porosity range of 14-19%. Pore sizes can vary, where intra-granular porosity results in larger pore spaces present in the samples. Following the Dunham criterion[12] it is classified as a calcite cemented grainstone, with the grains consisting of oolites and fossil fragments. Often these grains are in the order of mm's up to 3 mm. The mineralogy consists of 99 % calcite with 1 % quartz [9].

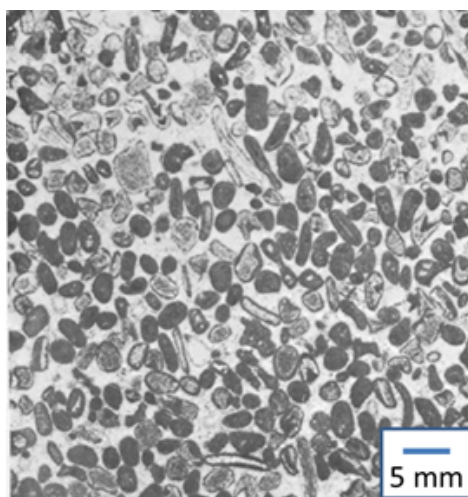


Figure 3.6: Thinsheet showing the Indiana Limestone structure, where the grains are cemented with calcite. [38]

3.2.4. Benin granite

The granite is mined by Adeoti SARL from the Dan quarry mine in Benin. No literature is available about this granite. This rock was examined microscopically to research the structure and the mineralogy. In Figure 3.7 thinsheets are shown, where in A and B an example is shown of the structure found in the Benin Granite. No porosity was found. It is possible that there is some porosity in the fractures, which where present in some of the samples. The main mineralogy consists of: 60% quartz, 20% microcline, 15% plagioclase and 5%biotite. The crystal sizes where found to be inconsistent and differs a lot with the mineral type. The crystal sizes varied from 30 μm to 800 μm for the main minerals. The plagioclase showed strong weathering with some muscovite enclosed in the minerals, this can influence the strength of the crystals. The muscovite is parallel and perpendicular in orientation relative to the twinning planes of the plagioclase as shown in Figure 3.7 C. In the biotite some muscovite was present. Azezorical some zirkone is present in the biotite, from which the uranium decay present in zirkone causes pleochroic halos [30] as can be seen in Figure 3.7 D.

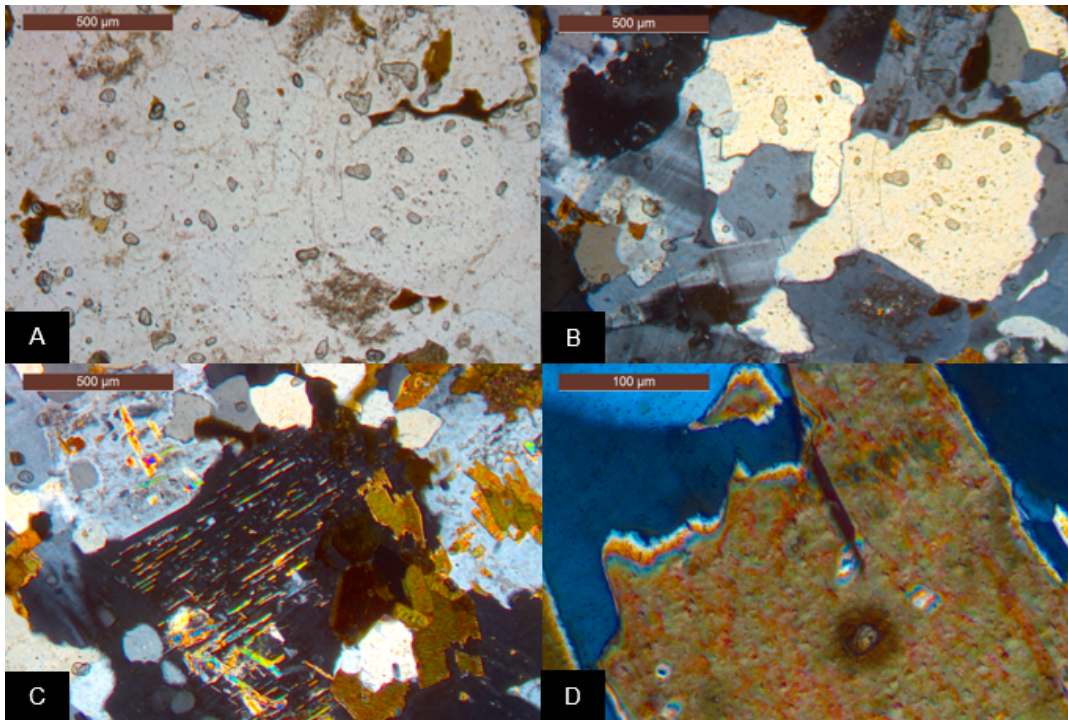


Figure 3.7: A. Plane section of the Benin granite. The brown coloured minerals are Biotite. In the thinsheet some airbubbles were captured which are visible on top of the crystals. B. Same section but polarized to identify quartz, microcline and plagioclase minerals. C. Polarized section where orientated muscovite is present in plagioclase. Most orientations were found to be parallel to the twinning of the plagioclase. D. A zircon mineral in biotite. Due to Uranium decay in the zircon a pleochroic halo is visible around the zircon mineral.

4

Geomechanics

4.1. Stress-strain results

In this section the main geomechanical results are shown for each test where ultrasonic monitoring was applied, see Figure 4.1. Different sample sizes were used as well as different settings for the tests. The difference in stress-strain behavior due to different strain rates or varying geometries was relatively minor. In Appendix A a table is provided of the sample properties and the associated test settings of the experiments used in this thesis.

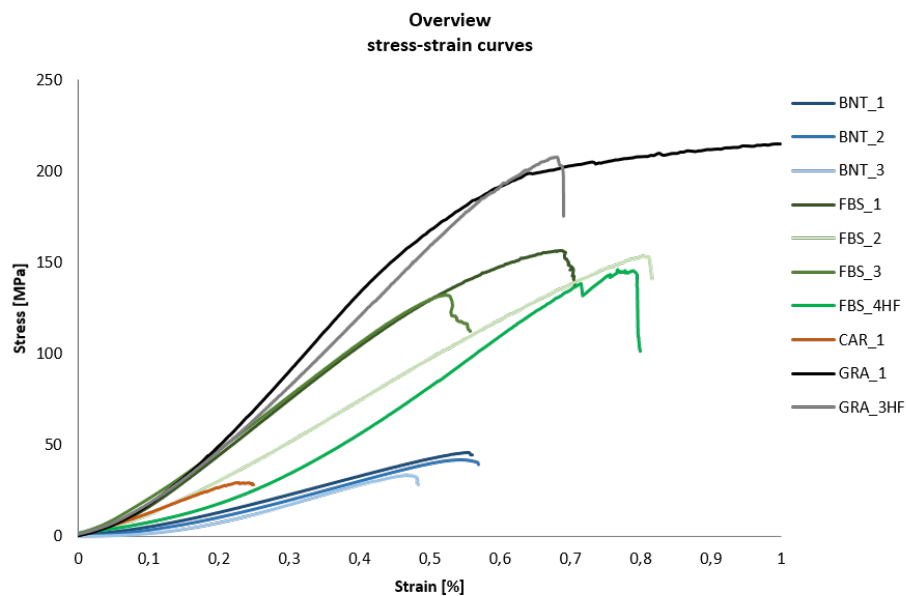


Figure 4.1: Stress-strain curves of the different test analysed with CWI.

In Figure 4.1 not the whole stress-strain curve is shown of GRA_1 to ensure the behavior of the other stress-strain curves are still visible, where the full curve is shown in Figure 4.2 a. The granite sample CAR_1 showed different behavior compared with the other samples tested. In contradiction to the other samples this granite sample showed no ultimate stress point but continued to deform with a linear trend for a second time with a more gentle slope than the elastic region. No ultimate strength point was reached, as this test was stopped before failure occurred.

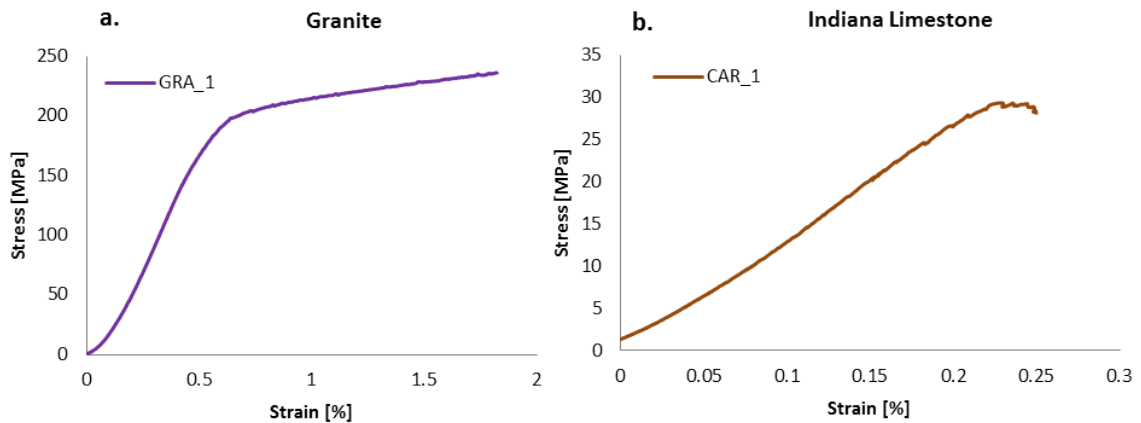


Figure 4.2: a. Total stress-strain curve of the GRA_1 dataset *replace with other dataset?* b. Stress-strain curve of the CAR_1, Indiana limestone, showing the notching behavior.

The Indiana Limestone showed 'notching' behavior while under compression, especially after the linear region as can be seen in Figure 4.2 b. Only incidental and less profound notches were observed in the sandstones and granites.

4.2. Discussion

Overall the stress-strain tests showed similar stress strain curve behavior as was seen in the rock mechanics theory chapter. Most curves show a smooth stress-strain curve, similar to the curves found in literature, where the main phases can be identified as was described by Brace, Bieniawski and Hallbauer et al.

Except for GRA_1, all of these tests attained a peak stress, short period of strain softening and finally rupture (shear or vertical failure). This type of behavior is classified as the brittle faulting regime [32]. The GRA_1 differed in the final stage of deformation, where no peak stress was reached. This process can be described as strain hardening in the post yield region. Only this sample of the Benin granite showed a long phase of strain hardening [32], while similar strain rates and sample geometry were used. In Literature this type of behavior was not found for brittle rocks while uniaxial compressed, thus an experimental error should be taken into account (for example bad contact of the LDVT). The only difference with the other granite samples was an existent fractures present as shown in Figure 4.3. This Fracture could possibly act as a plane of weaknesses preventing such a long phase of strain hardening.



Figure 4.3: Fracture present in GRA_2. A similar fracture was present in GRA_3.

The 'notching' in Figure 4.2 b., was not found to be well-described in literature of rock mechanics. Bogusz and Bokuwska touched on the subject and described this notching as a local decrease in stress, due to cracks in the pre-critical phase before the rupture [5]. What can be seen in the CAR_1 data is the rate of displacement,

by looking at measurements taken in a strain interval. In Figure 4.4 this was done by projecting the density of the acoustic measurements on the stress-strain diagram.

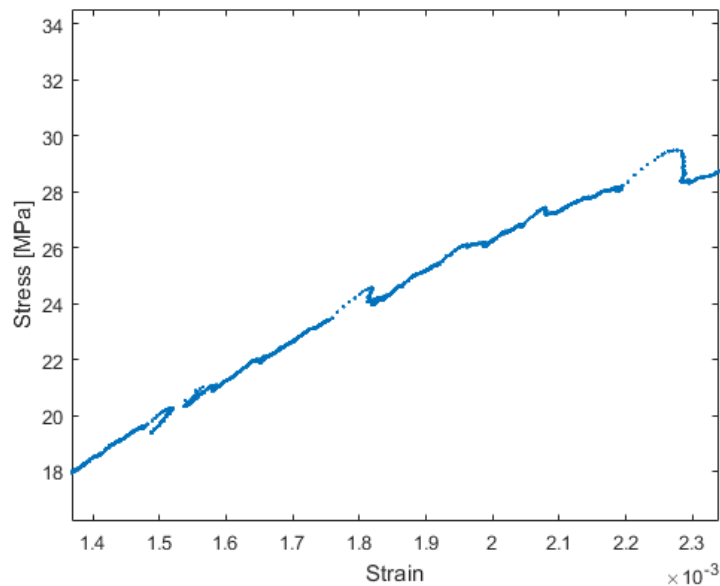


Figure 4.4: Zoomed in section of the notching of the stress-strain curve of the CAR_1 dataset

This shows that during a notch less data points are taken, resulting in an inconsistent strain rate executed by the compression testing machine. Especially for larger displacements in a short time span this effect in the stress strain curve will be present. In the Indiana Limestone larger pores and grains are present which can be looked at to explain the notching behavior. Baud et al. described two phenomena which resulted in larger strain variations due to compressive testing in high porosity carbonates: pore collapse and grain crushing [2]. But for both phenomena an effective stress is needed which is lacking in the uniaxial compression test performed. A possible theory for the notching behavior is that individual cracks (the classical Griffiths cracks model) are activated at sufficient size that the change in strain is too large for the machine to maintain the constant strain rate (Response system). This complies with the notion from Hallbauer and Lockner that post failure microcracks are formed on the size of flaws on the scale of the grain size [24] [20], which is in the order of mm's for the carbonate. Similar notching behavior was also found by Yang et al. when pre-existing larger flaws were present in a rock [46]. when the energy threshold was reached of these flaws during compression a notch was formed.

5

CWI

5.1. CWI results

In this section the CWI results are shown, retrieved from different methods of CWI analysis which were applied to acoustic data sets. First a Bentheim dataset, BNT_3, is used to show what results were encountered when different settings were used. The different settings are: fixed reference, rolling cross correlation, window position, window size and correlation lag size. This will then be followed by several other datasets, monitoring different lithologies and with different source frequencies.

5.1.1. Reference points in cross-correlation

Fixed reference point

In Figure 5.1 b. and Figure 5.1 c. the effects are shown when different reference points are used in the CC as proposed by R. Snieder. Two different stationary points were chosen with which each time window of the received acoustic signal is correlated. In Figure 5.1 b. a fixed reference point was used at the start of the experiment, thus in the crack closure phase as described in theory Section 2.1.1. An example of the acoustic wavelet is shown in Figure 5.1 a., where the correlation windows used are indicated with colour bars. With increasing measurement number a correlation curve is obtained where the colour of the curve corresponds to the window used.

In Figure 5.1 b. all windows show a decline at the beginning of the test. After this decrease, smaller alternating increases and decreases can be seen in the cross correlation coefficient with no particular trend present between the different windows. Only the first window exhibits a peak at point 35. The CC coefficient is not very high for most of the figure; between 0.27 and 0.70. For comparison, when totally incoherent windows (by selecting different parts of the wavelet) were compared CC coefficients were found to be as high as 0.5.

In Figure 5.1 c. the same dataset is used, but now a fixed reference is picked at measurement point 35. This measurement point was taken in the elastic region as shown in Figure 2.1. All windows show a smooth decrease of CC with different slopes until approximately measurement 48. Window 1,2 and 3 continues to decrease in a smooth way. The other windows further in the coda show a clear change of slope at measurement 38. As well as the fixed reference point at the start this figure shows low CC coefficients at the second half of the experiment, except for the first window consisting partly of first arrivals.

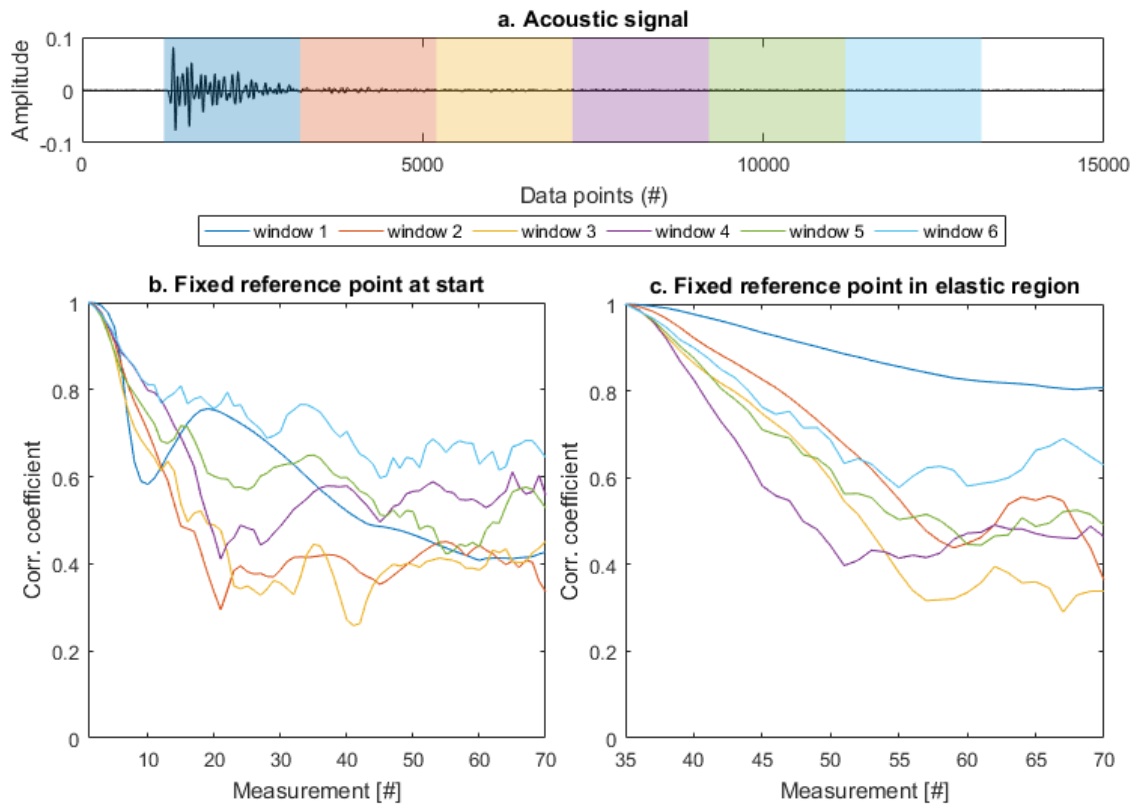


Figure 5.1: a) Example of a scattered wavelet, where the correlation windows are indicated by colour bars. The x-axis is in data points. b) CC where the first measurement is taken as a reference point. c) CC where measurement 35 is taken as a reference point, which is in the elastic deformation region.

Rolling Cross Correlation

In Figure 5.2 the same dataset with the same variables was used but processed with the RCC as shown in equation 2.2. Another type of curve is now obtained, where there is not an overall decrease of CC coefficient as was seen when the CC was used. In the beginning all the curves show some erratic decreases and increases of the correlation coefficient, which are in phase with each other. The first window consisting of first arrivals shows less sensitivity, only a small drop is observed at the end of the experiment. For the other windows a sort of plateau is observed between measurement 30 and 50. At approximately point 50 there is a decrease in the CC. Especially window 2 shows a clear plateau and decrease in correlation coefficient. The three windows which are the furthest in the coda area, window 4 until 6, show more erratic behavior.

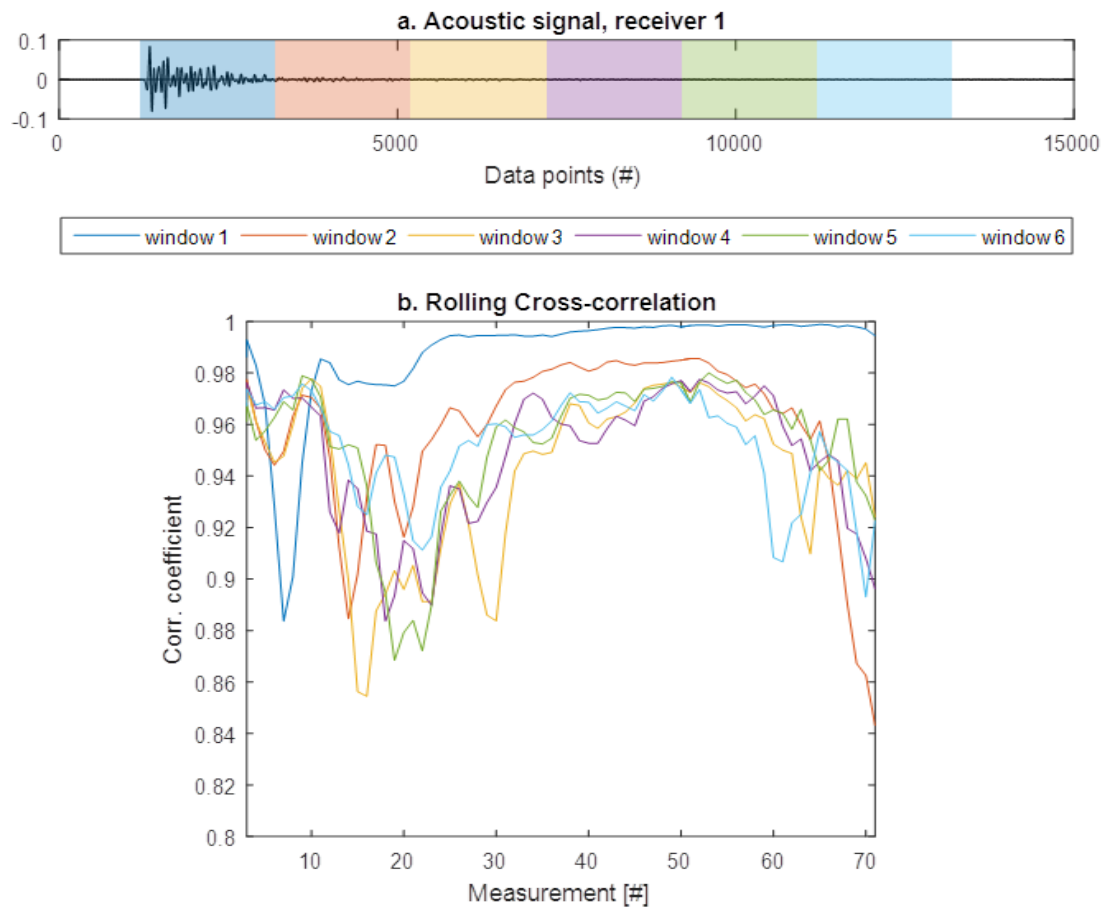


Figure 5.2: Rolling cross correlation used with a lag distance of 1 measurement. a) Example of acoustic wavelet recorded during the test, where the correlation windows are indicated by colour bars. The x-axis is in data points. b) Cross-correlation coefficient vs ultrasonic measurement.

5.1.2. Location of receivers

As shown in Figure 3.2 the receivers were located at three separate locations, one axially and two radially. In Figure 5.3 the results are shown for these different positions. Receiver 1 is the receiver at the bottom housed in a stainless steel cup, receiver 2 and 3 are housed in PEEK casualls placed radially opposing each other. The same window lengths are applied, though the starting location differs due to a short travel time difference. One of the main differences between the received signals is the amplitude, which is much lower for the radially mounted receivers. The first arrivals are less apparent in the side receivers, resulting in a less clear distinction with the coda. Although the distance is equal for both side receivers, the coda waves shape differs due to receiving different scattered waves.

At a lag of 1 a dip in CC can be observed at measurement 17 and 21, which are a result of sensitivity change on the monitor. These points can be disregarded though they do show the importance of constant source and receiver settings for experimental testing. In contradiction to the RCC results of the bottom receiver, all windows of the side receivers show a more apparent decrease in the CC coefficient after measurement point 50. For the side mounted receivers a slight increase is visible from the start, with a plateau between measurements 35 and 50. The overall decrease after the plateau is visible from point 50 for all three receivers, see Figure 5.2.

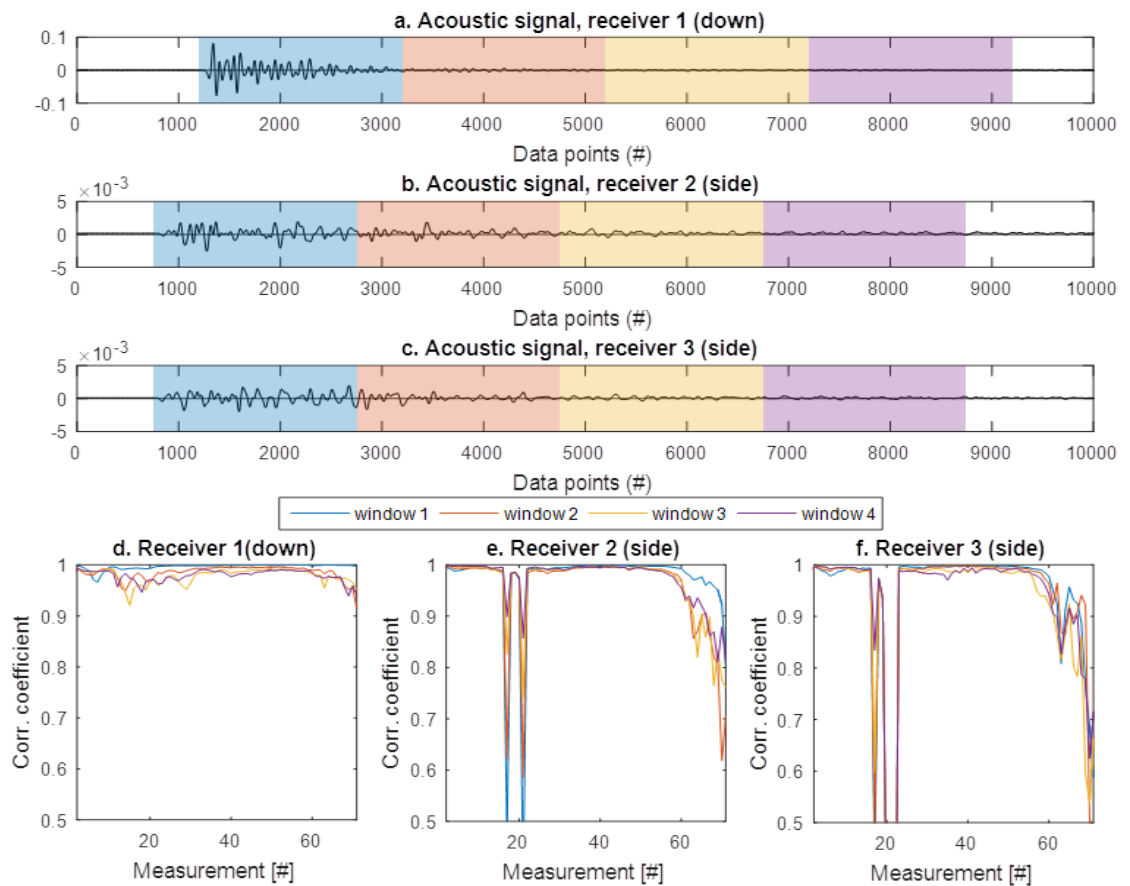


Figure 5.3: These figures compare the RCC for the different receivers. A correlation lag of 1 was used. a. Example of acoustic wavelet of the lower receiver. b. and c. Examples of the wavelet of the side receivers. d. CC curves of the acoustic wavelets retrieved at the bottom receiver. e. and f. correlation coefficient curves retrieved at the side receivers. The curves correspond to the colour bars of the windows of their acoustic signals.

5.1.3. Correlation lag

The timestep used in the rolling cross correlation is one of the factors which determines its sensitivity to changes in a medium. In Figure 5.4 b. the effect of different lags is shown for the Bentheim sandstone. A low strain rate was used to ensure that there is enough room to vary the lag. A lag of 1, 3 and 5 are used to show the effect of change in the curves. In this figure, the outliers explained in the previous sections are visible between measurements 17 and 25 (at different locations due to the lag difference).

The main difference between lag size, for instance comparing with a lag of 3 with a lag of 1, is that the correlation number is lower for a higher lag number and it seems that the figure is moved to the right. However, this is not the case for the whole figure. The plateau starts at a later measurement point for a higher lag, but the decrease after the plateau starts at approximately point 48 for every lag which is an important feature. This results in a shorter plateau for larger lags, where the decrease is more apparent. Similar results were observed for the other receivers.

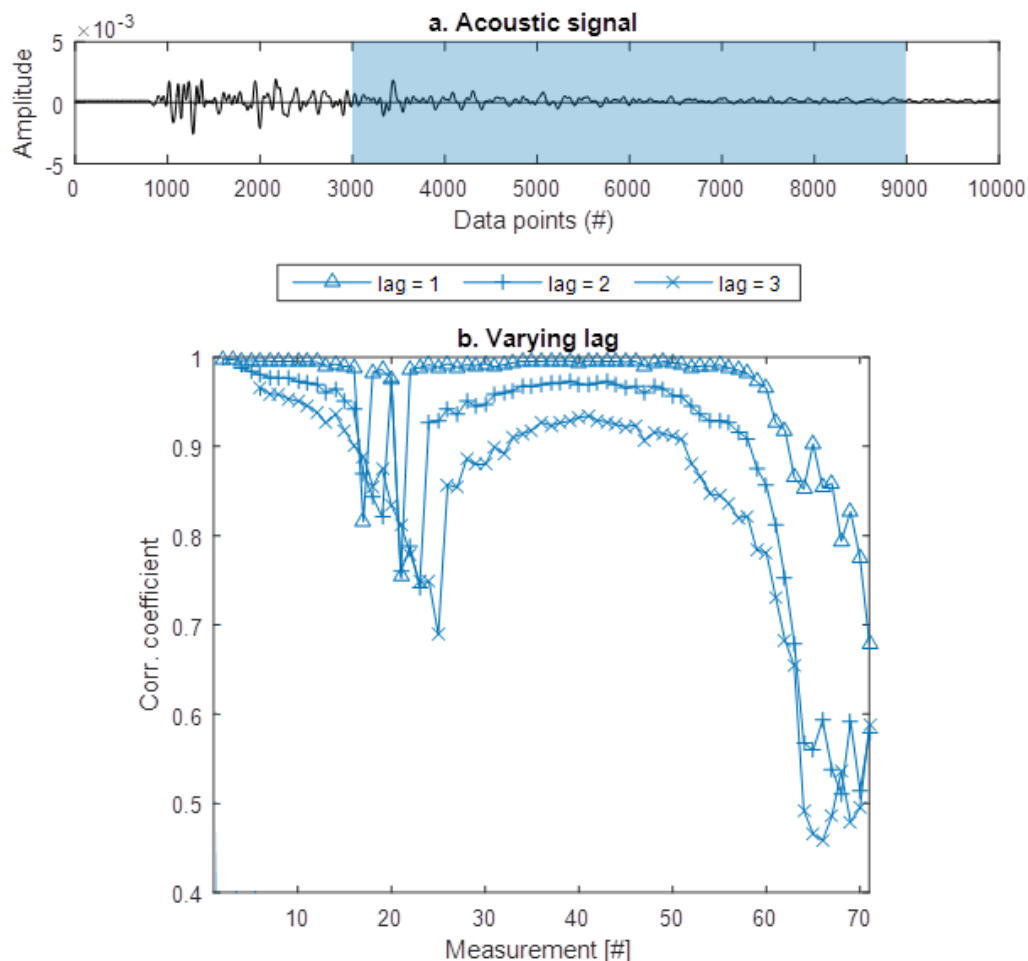


Figure 5.4: RCC results of different CC lag sizes for BNT_1. a. Example of acoustic wavelet to indicate the correlation window. The same window is used for every correlation curve b. Results of correlation curves, where each is indicated with different markers as shown in the legend.

5.1.4. Correlation window sizes and positions

Another factor investigated is the position and length of the windows used which are cross-correlated. In Figure 5.5 the results are shown for the BNT_3 side receiver dataset with three different window sizes. Four different sections of the wavelet are compared with a CC lag of three. The first part of the measurements has been disregarded in this case to focus on the plateau area and the decrease.

A decrease of CC occurs for most windows at approximately measurement point 50, except for the first one or two windows. At these windows the signal consists of earlier arrivals. If the window is taken too far into the coda, a less apparent dip in cross correlation number is found. When a small CC window is used, i.e. 500 data points, more erratic results are found. Because the amplitudes of the earlier arrivals are not dominant in the wavelet received at the side receivers, the total wavelet can be taken to observe similar behavior. The receiver in line with the source shows different results, with a clear coherent first arrival and subsequent exponential decay towards the coda. The amplitudes of the early arrivals are relatively much higher than the coda, resulting in an unclear decrease of cross correlation if the window covers the coherent arrivals only. Generally, the results show similar behavior for the different windows.

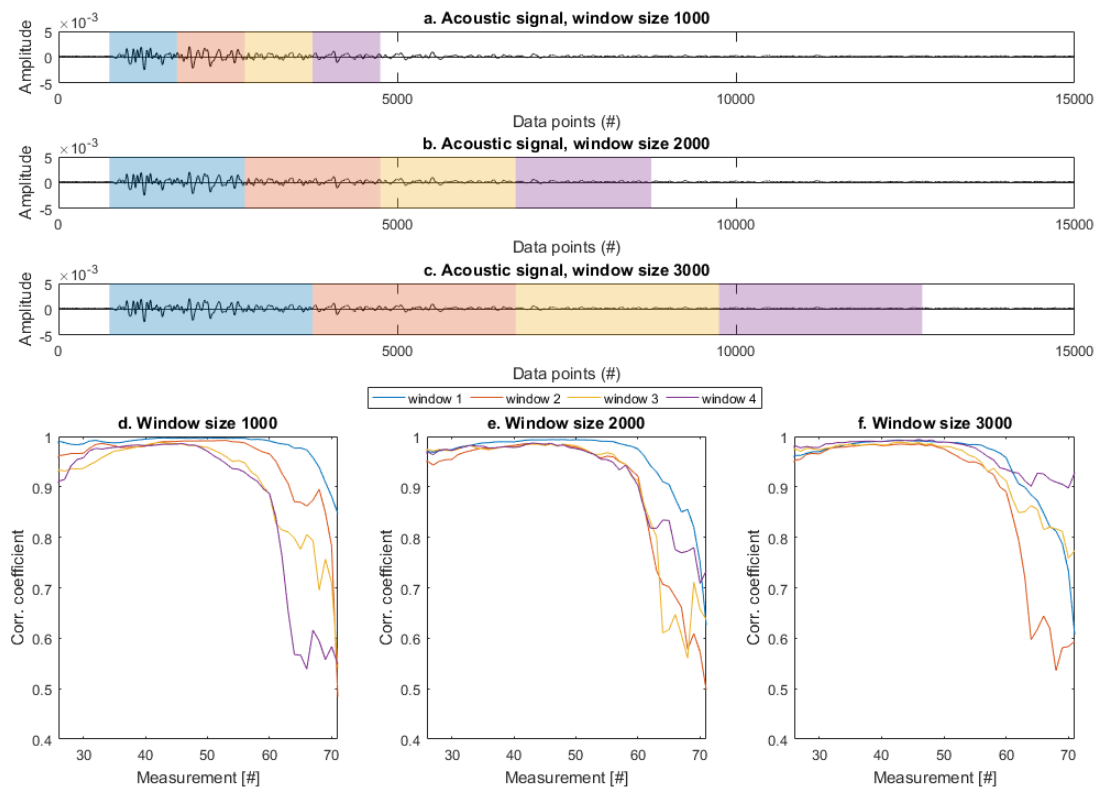


Figure 5.5: Results of different window sizes and positions for the BNT_1. Each curve is indicated with different colours as shown in the legend corresponding to the windows in a, b and c.

5.1.5. CWI with stress-strain curves

In this section the main results are shown when the CC curves are compared with the stress-strain data. The time of each wavefield and strain measurement point is recorded and this is used to align each measurement point with the corresponding stress/strain measurement in time.

5.1.6. Bentheim Sample

In Figure 5.6 the results are shown for the BNT_3 sample with various correlation lags. It can be seen that for a lag of 1 the plateau of the correlation curve is approximately at the the start of the linear section of the stress-strain curve. For the other lags the plateau is displaced with approximately the lag difference in correlation, which can be seen by looking at the length until the first nonzero value of correlation coefficient is obtained at the beginning of the curve. At a strain of 3.25×10^{-3} a decrease is observed for the curves with a lag of 4 and 7. When zoomed in this can be seen at the same strain for the curve where a lag of 1 measurement is used. This is approximately equal to the halfway point of the linear section of the stress-strain curve.

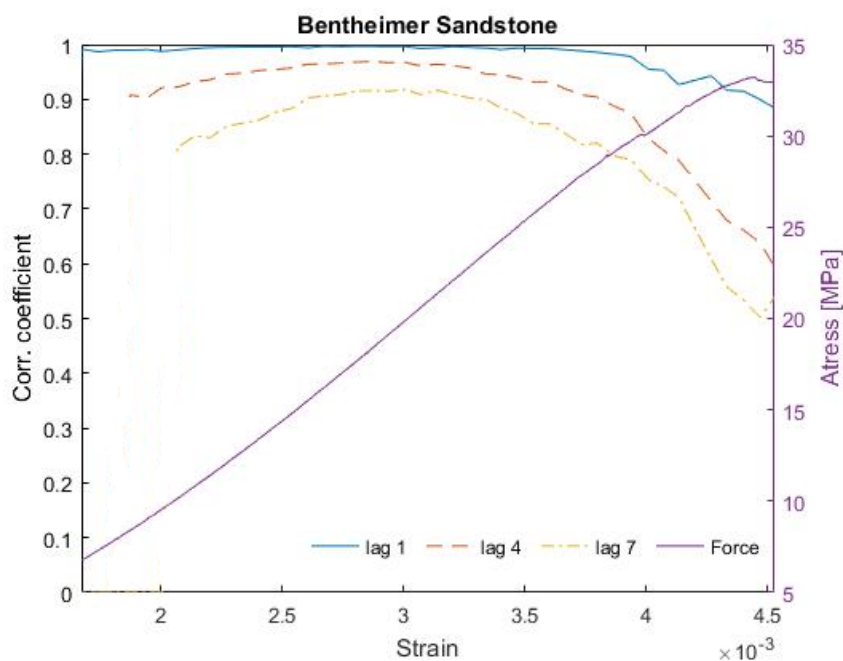


Figure 5.6: Results shown of a RCC curve of the BNT_1 dataset plotted against strain. The cross correlation number is on the left axis. In purple the stress-strain curve is shown, where the stress is shown on the the right axis.

5.1.7. Other rocktypes

In total four different types of rock samples were tested and an aluminum sample for reference. The different rock types tested are, three sedimentary rocks, from which two are sandstones, the Bentheimer Sandstone and the Fontainebleau sandstone. One carbonate rock was tested, the Indiana limestone. Finally a igneous rock was tested, a Benin granite. The acoustic and stress-strain data were processed in the same way as the Bentheimer samples. The source used is a 1 MHz or 2.25 MHz p-wave, which will be presented in the following sections

Fontainebleau Sandstone

In Figure 5.7 the results are shown of a Fontainebleau sandstone test, monitored with radially mounted receivers. In this figure three different coloured curves with different correlation lags are shown: lag of 1, lag of 4 and a lag of 7.

In this figure there is a less clear plateau visible as was seen in the previous Bentheim figures. The behavior is more erratic, especially for a larger lag. There is an overall decrease at a strain of approximately 5.5×10^{-3} .

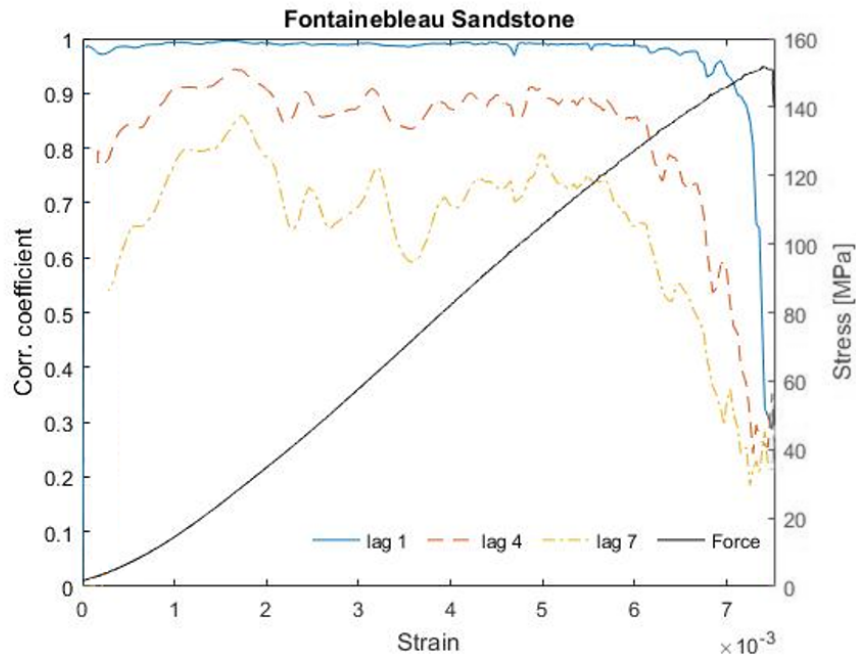


Figure 5.7: Cross correlation curve with stress strain curve results. Stress curve corresponds to the right axis. Cross correlation curves correspond to the left axis.

In Figure 5.8 a vertically zoomed in version of the curve with a correlation lag of 1 is shown. In this figure a plateau starts in the linear region of the stress-strain curve. The second half of the curve shows some interesting behavior. At a certain moment the curve becomes erratic with relatively larger drops, for instance the spikes at a strain of 4.7×10^{-3} and 5.5×10^{-3} . From this point onwards there is an overall decrease present in the CC curve.

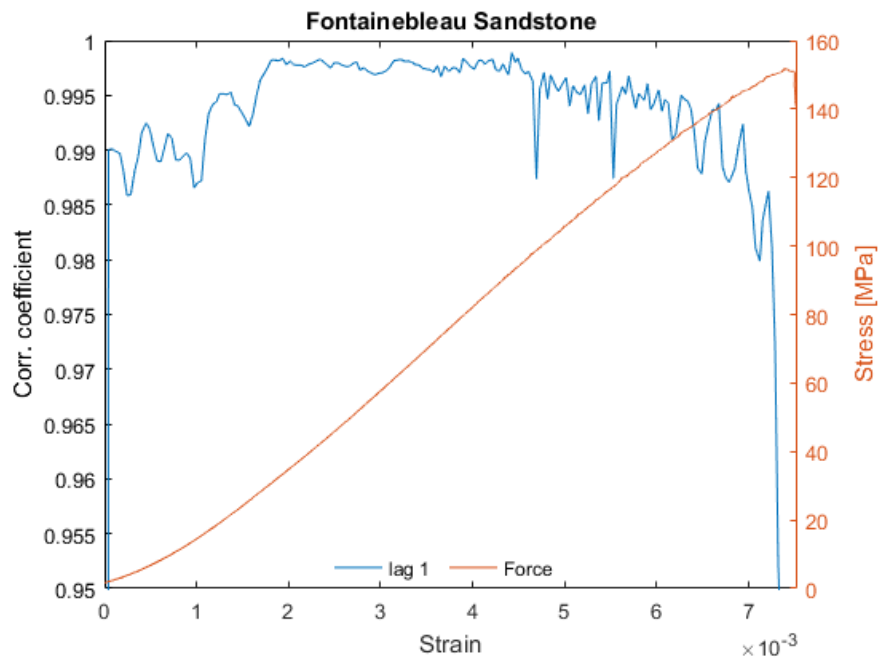


Figure 5.8: Vertically zoomed in results of the cross correlation curve against strain with the smallest possible lag for this dataset corresponding to the left axis. On the right axis the stress is shown vs strain.

Carbonate

The carbonate showed a different stress-strain diagram, with notching resulting from a rapid increase in strain accumulation in time, the 'notching behavior' as discussed in the geomechanics section. Much more acoustic measurements were taken during this test than the Bentheim sample, around 300 measurements were taken (in comparison with the 60 measurements taken during the Bentheim test), see Figure 5.9. Due to this larger amount of measurements much smaller correlation lags over strain can be taken.

For the correlation lags of 50 and 80, the Indiana limestone shows similar behavior when compared with the Bentheimer sample. For the correlation lags of 4 and 10, similar behavior can be seen as with the Fontainebleau sandstone shown in Figure 5.8.

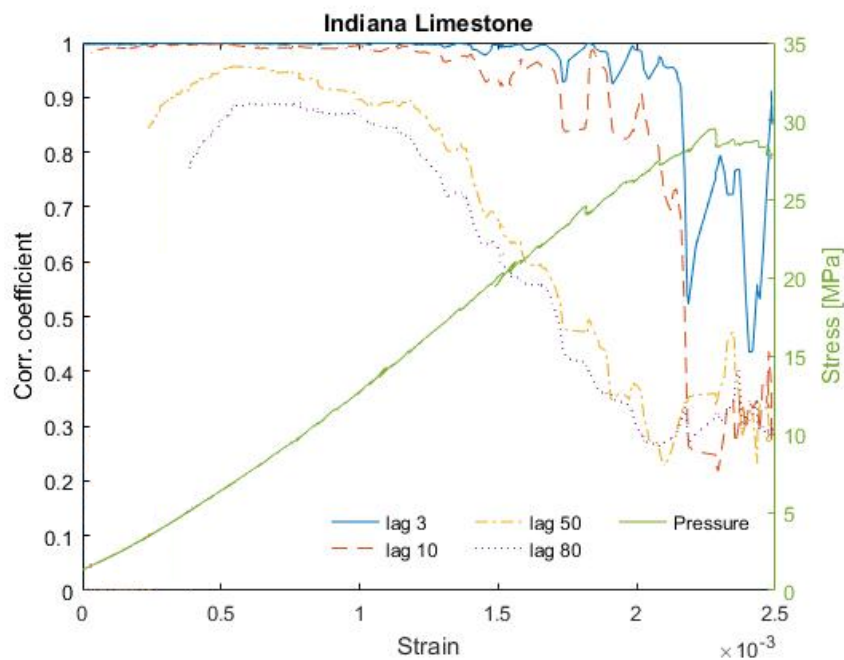


Figure 5.9: Results of the Car_1 sample (Indiana Limestone), with RCC on the left axis and stress on the right axis.

In Figure 5.10 a strongly vertically zoomed in version of the cross correlation curve with a lag of 1 can be seen. The smallest possible lag of 1 is used to show the small scale correlation behavior of the rock. The stress-strain data is shown only at the places when an acoustic measurement is taken. Similar to Figure 4.4 this visualizes the change in strain over time, because each acoustic measurement is taken 15 seconds apart from each other. The Figure shows that when such rapid change of strain takes place a peak of lower cross correlation number can be seen slightly beforehand. Some examples are shown with black dashed lines for clarity. The amplitude and number of these fluctuations increase towards the failure point of the rock sample.

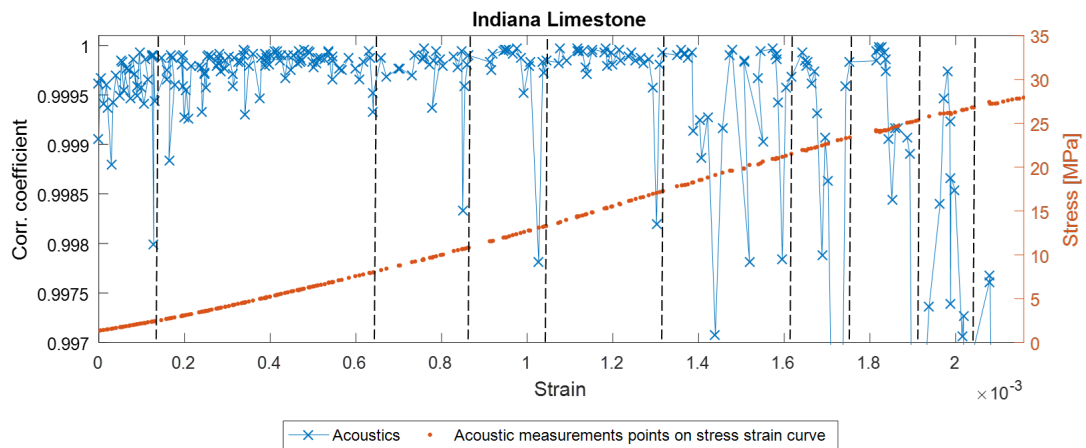


Figure 5.10: In orange the stress-strain data is shown only at the points where a measurement is taken acoustically. The strain rate is more rapid when spacing becomes larger between the measurement points.

Granite

The GRA_1 test showed no rupture, resulting in a different type of stress-strain curve. In Figure 5.11 the results of the RCC and stress curve are plotted against strain, where the shape of the RCC is different than seen before. There is an overall increase until approximately a strain of 0.005 for all three lags. There is no clear plateau at the linear part of the stress-strain curve, more a drastic increase in cross correlation number displacing to the right for larger lags. At a strain of 0.008 the correlation number stays almost constant.

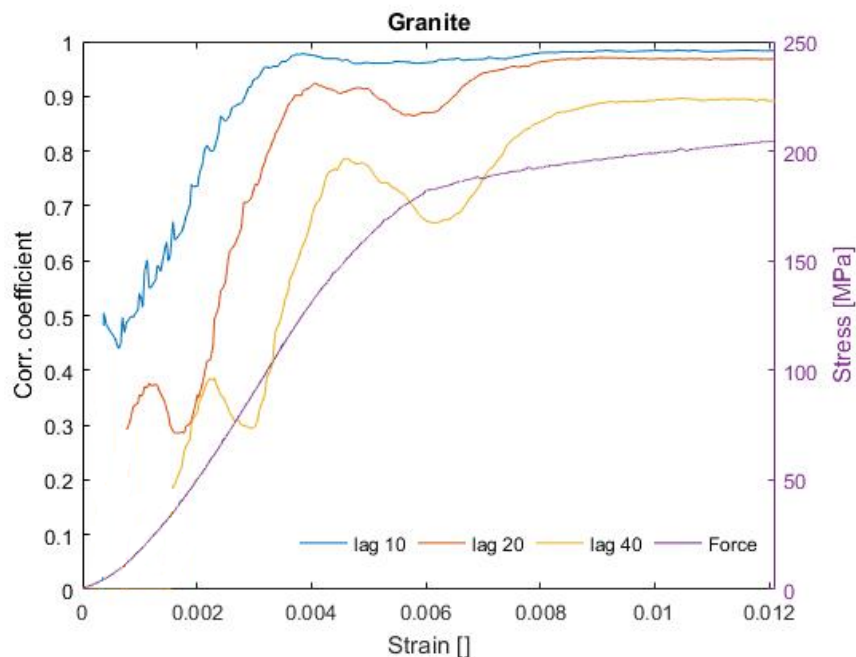


Figure 5.11: Various CC lags plotted against the stress-strain curve for the GRA_1 dataset.

5.1.8. Change in source frequency

All previous test were done with a 1 MHz p-wave source. A 2.25 MHz p-wave source was used to see what the effect is of using a higher frequency. First this was tested on a Bentheim rock, where a radial mounted receiver was used. For this an amplifier was used to ensure enough signal was received. This was the only test showing a dominant low frequency along the total wavelength as can be seen in Figure 5.12, which was processed with a high-pass filter before cross-correlating. This low frequency was only visible when the extra

amplifier was used. In Figure 5.13 the RCC is shown when a lag of 1 measurement is used, where the cross correlation number is plotted against measurement (an error occurred resulting in a corrupted time-string). This dataset is included because there are some interesting features which will be discussed in relation to the frequency sensitivity. The Indiana Limestone was not tested with a higher frequency source due to its high sensitivity of RCC during the 1 MHz test.

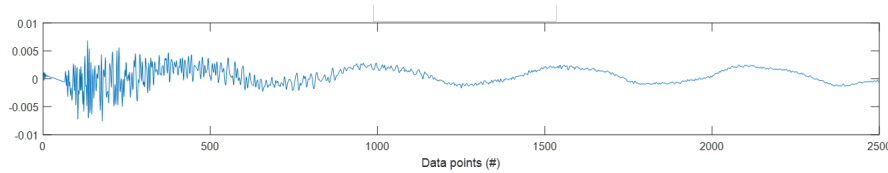


Figure 5.12: Wavelet from the high Frequency dataset with dominant low frequency before data was processed with a high-pass filter.

The overall behavior may seem similar with the Bentheimer sets tested with lower frequencies. However, the change in RCC is much higher over time, resulting in a much lower CC when larger lags are used. Another difference is that the behavior of the RCC is much more erratic, resulting in local drops.

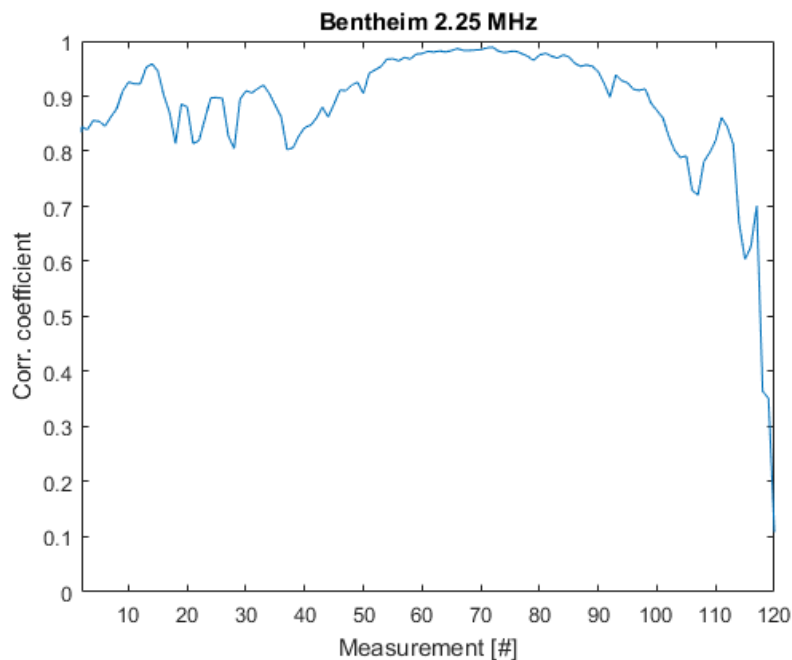


Figure 5.13: Result of the cross correlation number plotted against measurements for a Bentheimer sample. A filter was used to filter out the low frequency caused by the amplifier. A correlation lag of one was used

In Figure 5.14 the results are shown for the Fontainebleau sandstone when a high frequency source is used. The stress-strain curve is shown in yellow, where the acoustic measurement points are indicated with black marker points.

A short plateau is visible at the beginning of the linear region, while the overall behavior is erratic. There is an increase in amplitude of the peaks from this plateau.

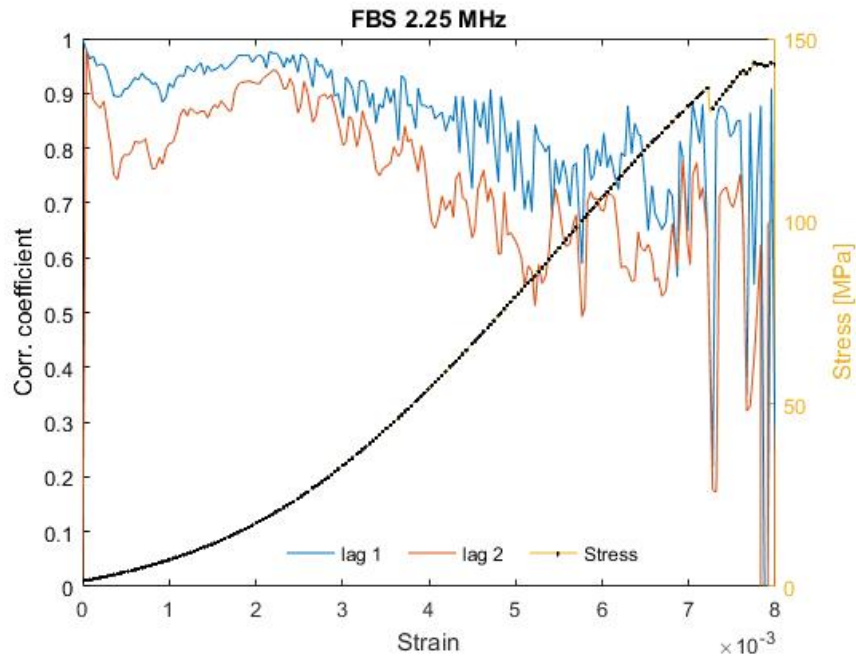


Figure 5.14: FBS_2 dataset for a lag of 1 and 2. RCC (left axis) and stress(right axis) is plotted against strain. With black points the acoustic measurement density are shown on the stress-strain curve.

In Figure 5.15 the results are shown from the GRA_3 dataset. This test was done with one bottom receiver due to a lack of high frequency receivers. The higher frequency results are different from the lower frequency results as shown in Figure 5.11. The results are comparable to what was seen with the low frequency Bentheim, Fontainebleau and Indiana limestone, with an increase in RCC visible towards a short plateau for the lag of 30. For the lower lags of 5 and 10 longer plateaus are visible. The Granite tests showed a larger variance if a different window position and length was chosen than the other rock samples.

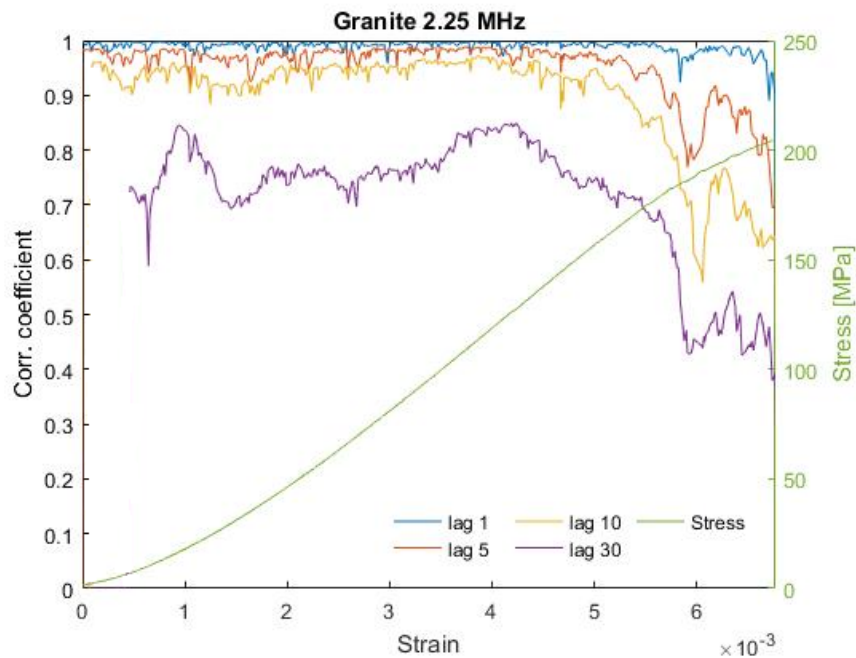


Figure 5.15: Results shown for the GRA_3 dataset for four lags. Correlation coefficient (left axis) and stress (right axis) is plotted against strain.

5.1.9. General results overview

In Figure 5.16 the four lithologies are shown in one figure. To display all figures in the same RCC range a similar acoustic measurement density (50-70 measurements) was used over the stress strain diagram with a lag of 1 measurement from initial loading to max peak strength. The Fontainebleau (1 MHz), Indiana (1 MHz) limestone (1 MHz) and the granite (2.25 MHz) dataset were reduced in measurement number to the lowest measurement number dataset of the Bentheim. In Figure the 5.17 the stress-strain curves are displayed with acoustic measurements taken as well as the yield point indicated with a larger red marker. This yield point was handpicked by eye approximately at the end of the linear region as was explained in the Rock Mechanics Theory. The same point is highlighted out in the RCC curves in Figure 5.16. In Appendix A each stress-strain curve is shown with its corresponding RCC curve separately on its own scale for clarity.

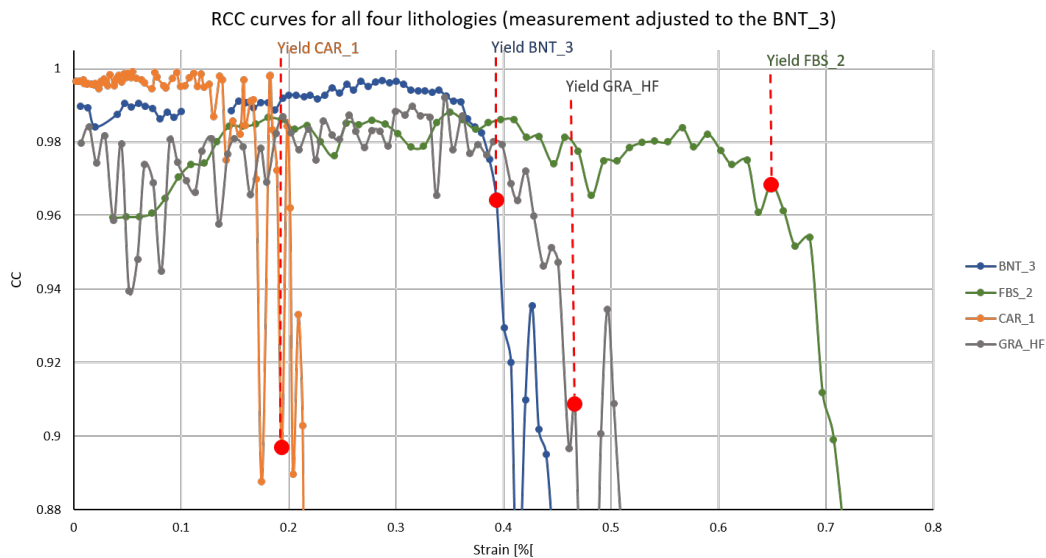


Figure 5.16: RCC curves for the four lithologies displayed versus strain. The stress-strain yieldpoints are picked with the use of Figure 5.17. Indicating that all datasets show pronounced RCC decay prior to the identified yieldpoint

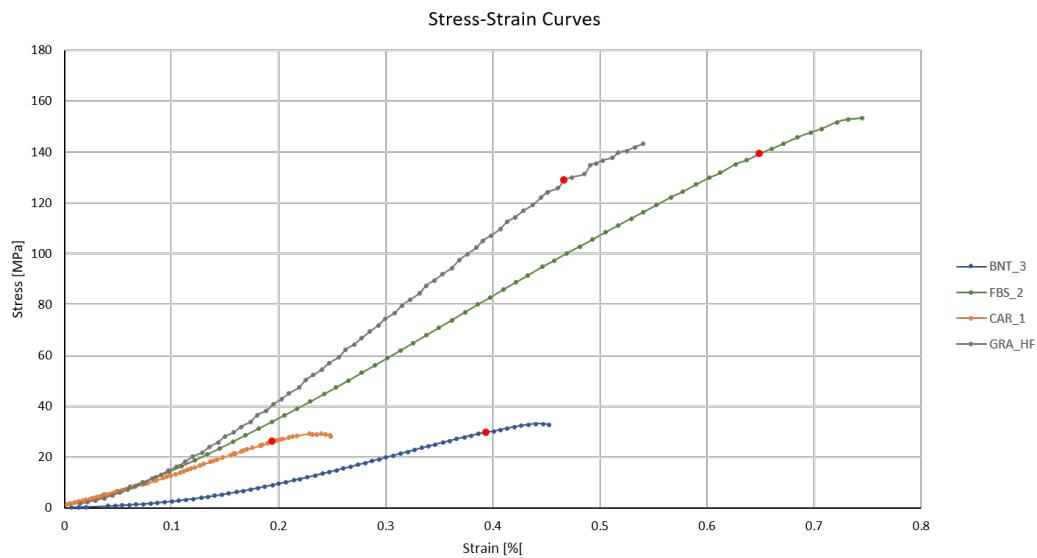


Figure 5.17: Stress-Strain curves of the datasets used for RCC analysis in Figure 5.16. With the red dot the handpicked yieldpoints is shown, Appendix A shows the independant stress-strain curves.

Although the individual behavior of each dataset is less clear by equalizing the number of measurement

points, it is interesting to see the similarities between the RCC curves of the different lithologies with respect to the geomechanical properties deduced from the corresponding stress-strain figures. Some general observations and remarks:

- By equalizing the measurement points over stress-strain to around 60 points, the range of RCC decay becomes in the **same order of size** but the erratic behavior is less clear. For example with the FBS_2 dataset, where the clear and frequent dips in RCC are not as apparent as in Figure 5.8. By reducing the measurement points the sensitivity towards individual events becomes less clear and smoother behavior is obtained.
- Roughly in each RCC curve where a rock is brought to failure an overall **rising phase**, a **plateau** and an overall **fall** of RCC can be identified. Where the rising phase is longer than the nonlinear fracture closing phase in the stress-strain diagram. Incidental dips are sometimes observed in the plateau, which can result in multiple plateaus. The falling phase shows either a smooth overall decrease or can be more erratic.
- Each curves shows an overall fall in RCC **before the yieldpoint** picked from the stress-strain curves. This fall is not always a single event as with the Bentheimer, but consists of separate localized falls as can be seen with the CAR_1 dataset.
- An increase in source frequency increases the erratic behavior. A low lag number and sufficient measurement points are needed to observe this behavior.

5.2. Discussion CWI

Before conclusions are made about the obtained results, a closer look will be taken at the time-shifted cross correlation. The actual change of an ultrasonic pulse in a deforming uniaxial compressed rock medium will be discussed. Finally some theoretical explanation will be proposed on how this behavior can be characterized for the different types of rock.

5.2.1. Cross Correlation Coefficient

In this sub-chapter the time-shifted cross correlation number will be discussed by looking at the behavior of a wavelet, which can change in various ways. These changes can have different influences on the CC number, which will be demonstrated with an example wave: a single sine wave. The following cases are used: lag (time-shift), amplitude change, stretch (higher frequency) and finally a comparison is made when the actual shape is changed. As can be seen in the figure only the two latter cases influence the correlation number. In each case the window is taken from 0 to 6π , to ensure that the total energy (total wavelet) is taken into account.

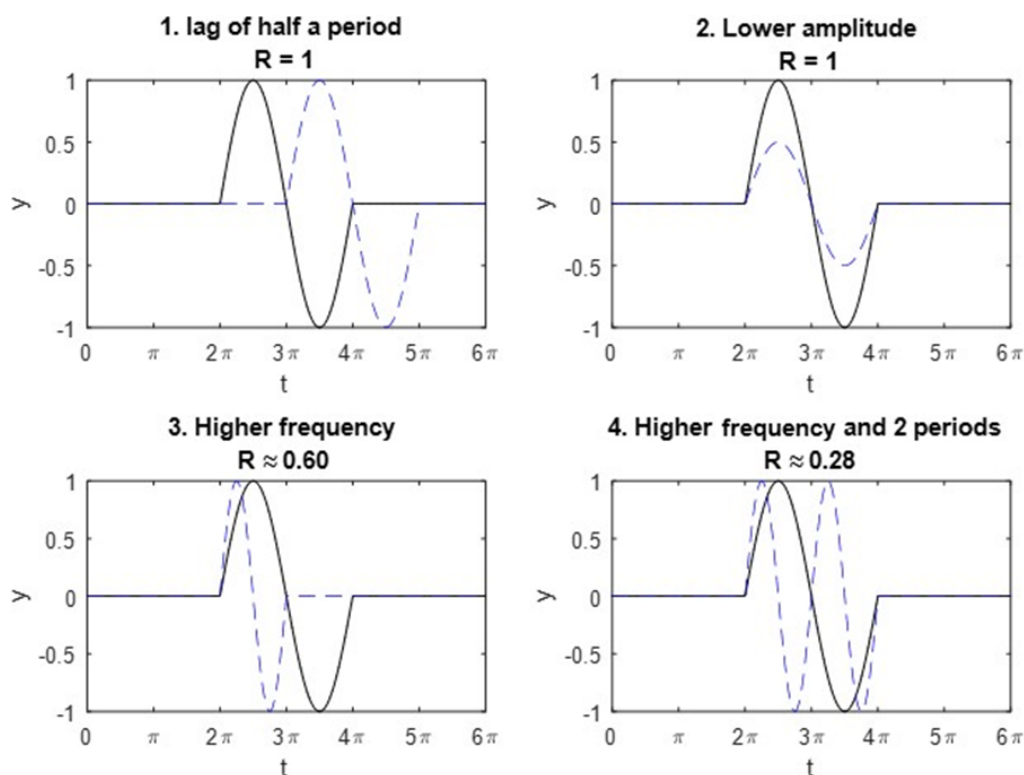


Figure 5.18: Effects shown on change of R when a wavelet is changed in different ways.

A lag or time shift of a wave, as shown in 5.18 (1), occurs when the total wave is displaced by equal amount. Gret, Snieder and Scales observed a time shift when compressing a medium [17]. This can occur when the wave traveled a shorter path than the original wave. A time-shift will have no effect on the CC when the same energy is compared in the correlation window. When a medium is compressed the total wavelet can be displaced, resulting in cross-correlating different parts of the wavefield in a fixed window. This effect can be negated by using a taper, which results in less focus on the boundaries with respect to the middle of the window. In practice this effect was hardly observable, because the influence of the boundaries are too small when a large enough window is used. The results are different when compared with a shorter correlation window where only the middle part of the wavefield is compared. However, the use of a taper can be important to ensure the boundary effects are mitigated when the type of change is closely studied.

Variation in amplitude due to energy redistribution is a commonly described phenomena in a changing

rock medium, which is linked with attenuation increase or decrease [44] [17] [1]. However, the time shifted cross correlation is normalized, so amplitude change is not taken into account in the CC as can be seen in 5.18 (2). However, uneven changes over a wavelet will be of influence on the CC number, because normalization takes place over the total wavelet.

Alteration 3 in Figure 5.18 can occur when the medium properties, bulk and shear moduli, are altered to a certain extent that the acoustic velocity increases, resulting in a higher frequency [28]. This effect was found to be relatively minor in the laboratory experiments conducted in this thesis.

Alteration number 4 is a total change of shape of the wavelet. This can occur for example due to a change in scatterers, resulting in a new wave path. Another possibility is the arrival of multiple wave modes at the same time, when travel paths undergo different changes, distorting the signal where the coda is a collection of scattered waves and different waves modes which will make it difficult to separate each part to a corresponding wave mode and/or scatter, as discussed in the theory section.

5.2.2. Acoustic scattering phases

In the results section roughly three phases can be identified in most RCC curves for the smaller lags, namely: the "rise"(Phase 1), "plateau"(Phase 2) and the "fall"(Phase 3). The rising phase can be irregular but there is an overall increase of the RCC which continues until a sort of plateau is reached. In the plateau phase, the RCC stays more or less constant. The third phase can be identified when there is an overall decrease of RCC, sometimes showing larger localized drops. Two types of behavior can be found in this phase, erratic behavior or smooth behavior. In this subsection a closer look will be taken at the wavelets themselves for each of these phases, for the different lithologies. In Figure 5.19 and 5.20 the axial and radial received wavelets are shown for the Bentheim dataset and their evolution in each phase. While there are some clear differences between the radially mounted and axially mounted receivers, we will focus here on the similarities in behavior.

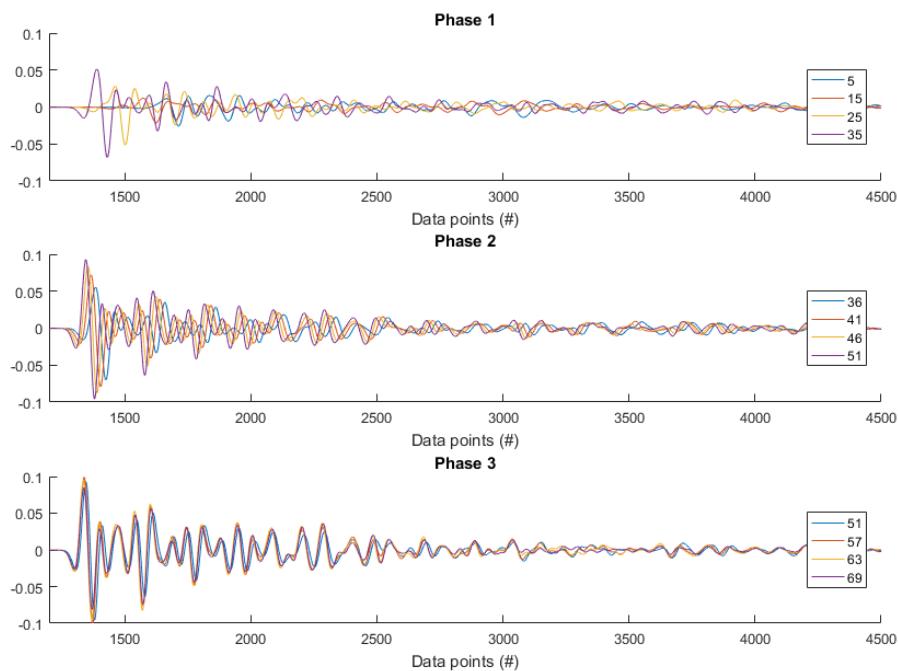


Figure 5.19: Bentheim receiver at the bottom placed in steel cups, thus in direct path of the source. The measurements are shown in the legend which are used to illustrate the behavior of the wavelet in the different phases

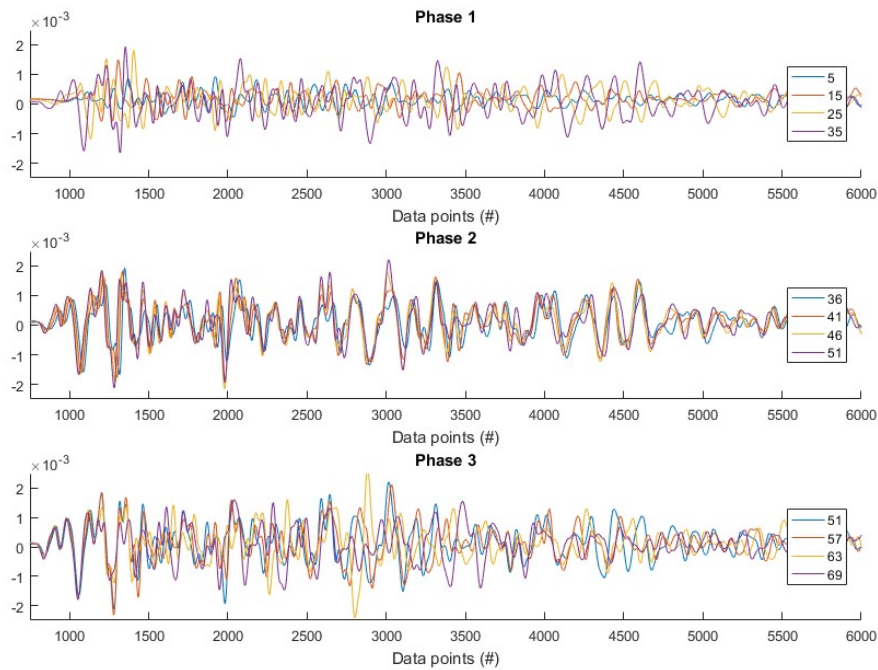


Figure 5.20: Bentheim receiver placed at the side. The measurements are shown in the legend which are used to illustrate the behavior of the wavelet in the different phases

By looking at the wavelets a window of highest sensitivity in coda can be chosen. The other lithologies could also be divided into three phases as shown in Figure 5.25. In each phase wavelets were chosen with equal distance to each other, so it can be imagined what will happen when these waves are compared with the RCC.

In **phase 1** there is a rapid rise in amplitude and shift to the left which can be attributed to an increase of coupling and closure of microcracks and flaws in the beginning of the test. This closure of microcracks can result in different scattering distribution inside the medium, resulting in irregular wavelets with respect to each other. This effect is best visible in the side receiver, because the influence of first arrivals and multiple arrivals is much smaller. When the wavelets are compared in this phase, it results in a lower CC coefficient. Due to the fixed correlation window, a large lag will result in a comparison with not the same scattering paths in the medium when there is a shift of signal. However, this effect will be small when using the RCC if a small lag is used and sufficient measurements are taken.

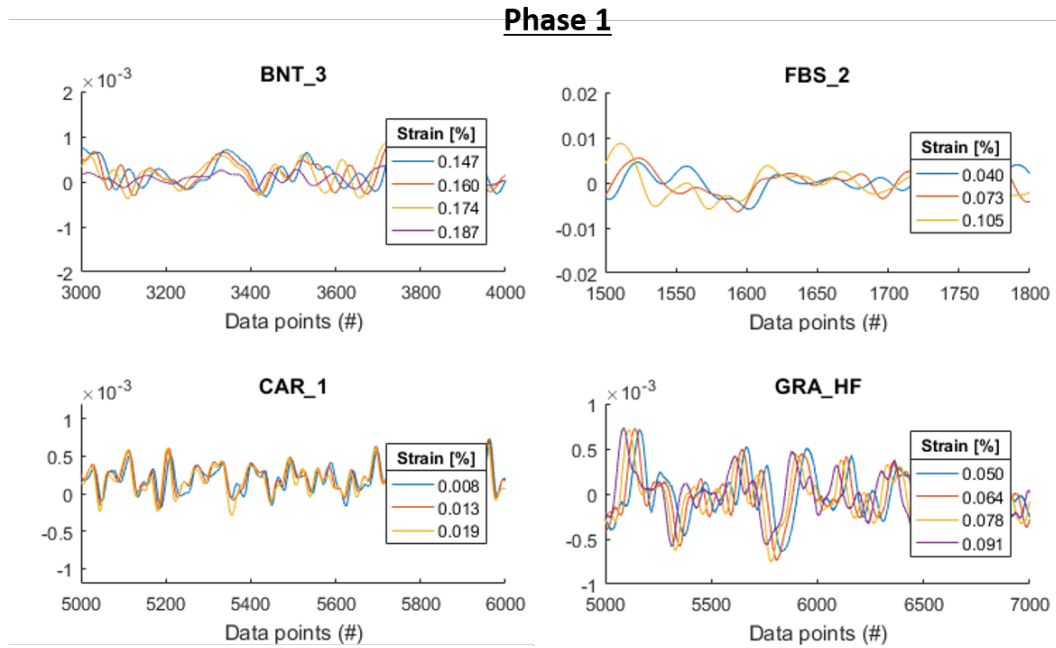


Figure 5.21: Zoomed in section of the coda for wavelets in the rising phase, where most samples show some incoherency between wavelets.

If we look at **phase 2** we can see that the shift and amplitude change is much smaller and more consequent in the bottom receiver. The side receiver shows even less change in shift, because it is less dependant on the axial compression. This phase shows hardly any change in signature of the wave, from which it can be deduced that there is little change taking place in terms of scatter distribution. In the RCC, only the changes in attenuation will results in varying amplitudes for the frequencies and thus a possible RCC change.

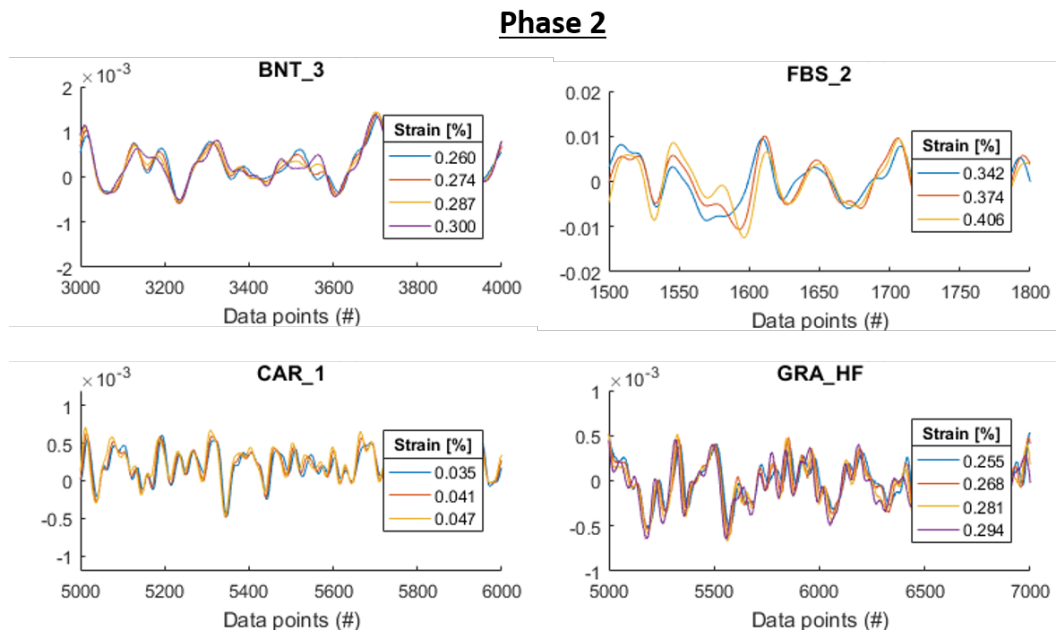


Figure 5.22: Zoomed in section of the coda for wavelets in the rising phase, where the wavelets show coherent behavior

In **phase 3** there is little to no shift and little decrease in amplitude if one compares to the first arrivals or multiples. However, there is very irregular behavior in the coda part for the wavelet in the side receiver. In the bottom receiver this irregular behavior can only be seen in specific parts of the wavelet for the Bentheimer

sandstone, for instance between data points 3100 to 3500. The side receiver is much more sensitive to the change in scattering, where the bottom receiver is more influenced by the coherent multiple arrivals.

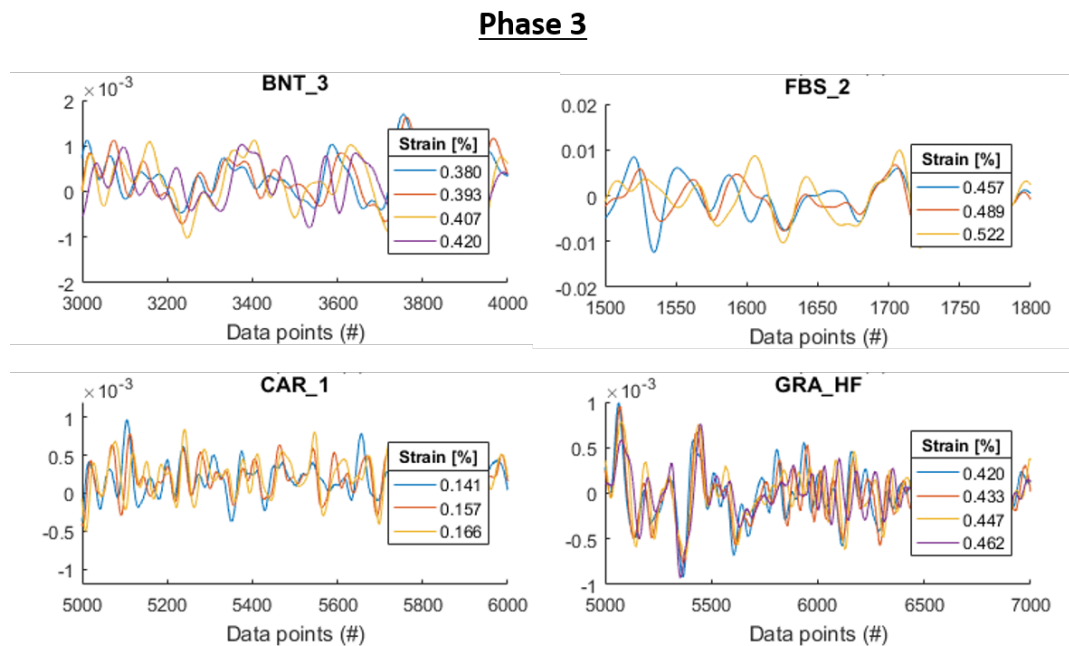


Figure 5.23: Zoomed in section of the coda for wavelets in the falling phase, where the wavelets show less coherent behavior as was seen in Phase 2 for the same strain differences.

A few general remarks when looking at the phases with respect to the RCC curves:

- The first arrivals for any lithology showed no change in phase 3, only until rupture occurred when there is no coupling anymore. This can also be seen in Figure 5.5, where the first one or two windows showed a much later dip in RCC than the windows placed further in the coda. In the side receiver the amplitudes of the multiple scattering is of sufficient size that the whole wave can be used in the correlation window. The highest amplitudes in the window have the most effect on the comparison when cross-correlated. In the bottom receiver the first and multiple arrivals are of large influence and should be avoided to observe changes in phase 3. The window to choose is dependant on lithology, sample size and the position of the receiver.
- In phase 3, two types of changes were found in the wavelet. The first is the decrease in amplitude. This change is often gradual and will result in a smooth gradual decrease of the RCC as was found for the Bentheim and low frequency Granite tests. The second type of change is the actual change of shape of the wave, which resulted in a sudden drop in the RCC. Both phenomena are often present for the different rock types and result in the type of behavior for the RCC curve in phase 3. The curves became less smooth when a higher frequency was used.
- The **lag number** used can be an important factor to detect transition to a successive phase. In the results where lag was compared it could be seen that the increase of the RCC to a plateau (transition phase 1 to phase 2) was found to be later in time for larger lag. This is due to the fact that the coherent waves of phase 2 are compared with the incoherent waves of phase 1. If a smaller lag is used the coherent waves of phase 2 will be earlier compared with each other, resulting in a plateau. In Figure 5.24 this is illustrated with two states compared with each other for a lag of 1 and a larger lag of 2. When a correlation is made between state B and A a RCC of 1 is earlier reached in the lag of 1 than 2, indicated with I. However, a decrease in similarity is found at the same moment, as can be seen by the lower RCC at measurement point 7 indicated with II. This was also seen in the results and can be explained by the relatively incoherent waves of phase 3 being compared with the waves of phase 2. There is less change in the waves in phase 2, so it does not have a large influence which wavelet of phase 2 is used

as reference to detect the approximate start of phase 3. This is only true if sufficient measurements are taken and the RCC lag smaller is than the plateau. The decrease seems less profound when a smaller lag is used, but all changes are less apparent if the same scale is used as with a high lag. When zoomed in, the different stages are clearly visible with a longer plateau.

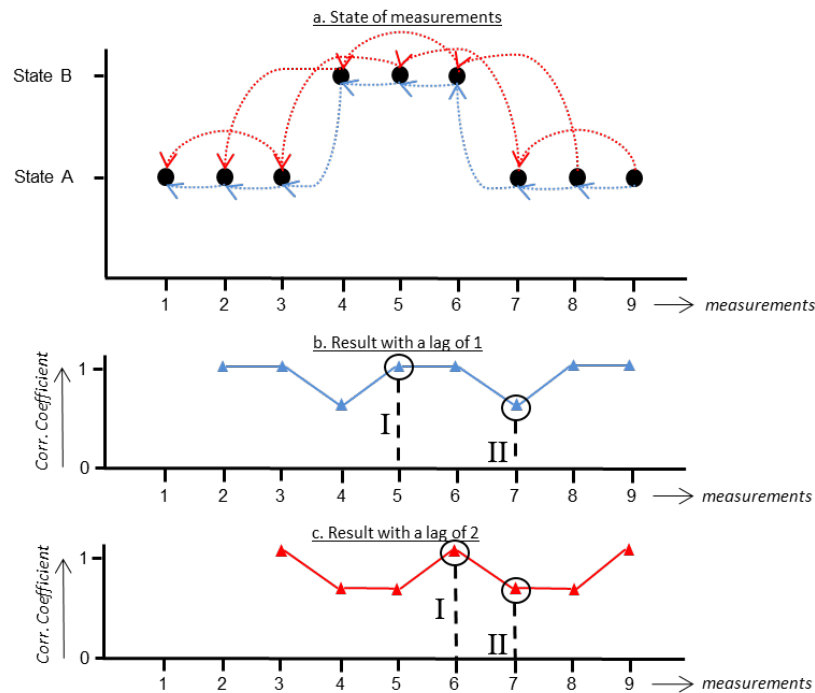


Figure 5.24: Schematic figure showing what effect the size of correlation lag has when compared between two different states.

The most dominating factors resulting in a change in the time-shifted cross correlation number are thus actual change of shape and unequal amplitude change of the wave. The latter means an uneven amplitude change of different parts of the wavelet in the RCC window. In the RCC with a small lag the waves are compared with waves which are still coherent to each other. When a CC is used with a fixed reference the changes are too large for a good representation of the wave behavior. In an compression experiment the total time shift in a wavelet will have influence such that not the same part of the wave is compared. The time-shifted CC will force a comparison even if two totally unrelated waves are compared. A more true reflection of the wave change in the RCC can possibly be made if a correlation distinguishes between uneven amplitude change and change in signature of the wave itself. For this a different method of comparison is needed than the time-shifted cross-correlation.

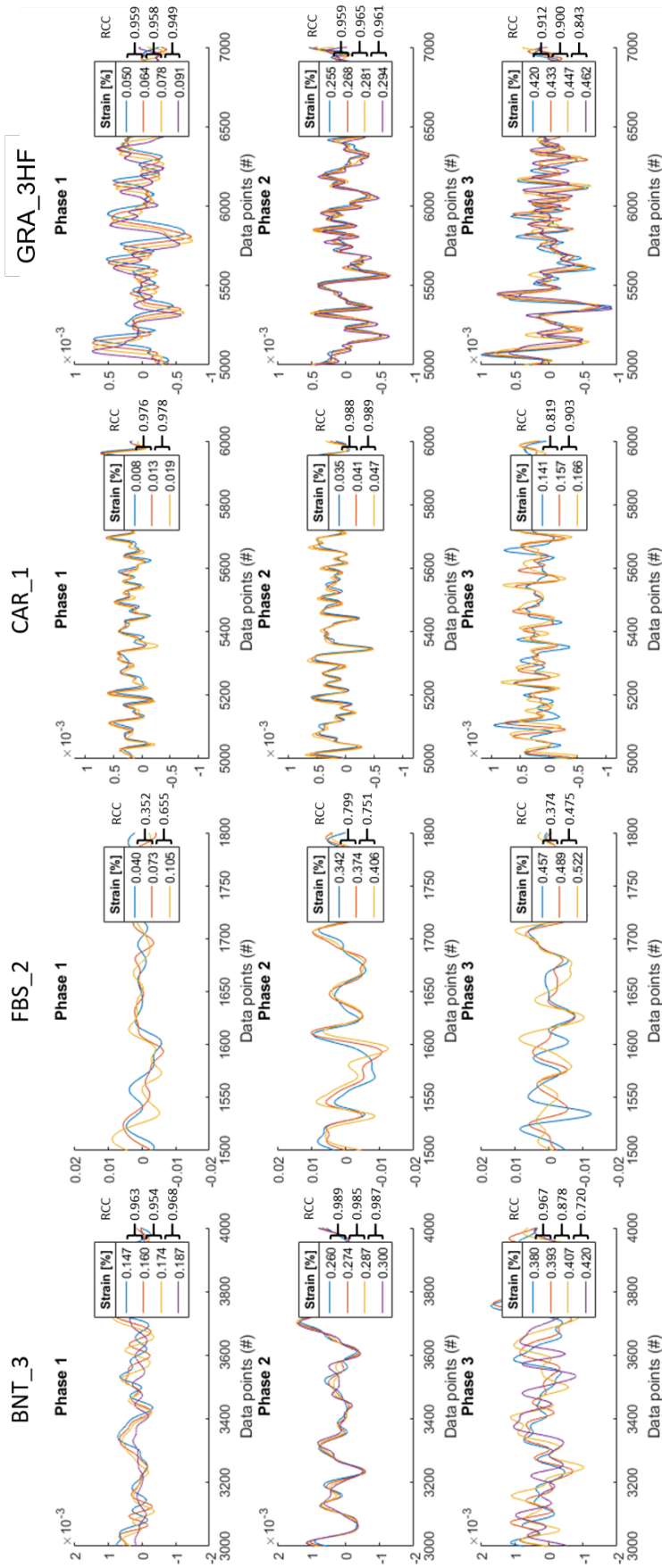


Figure 5.25: Zoomed in sections of coda of a Fontainebleau, Carbonate and Granite(High Frequency) dataset showing the three phases. The strain difference is kept equal between each of the wavelets of the different phases of the rock to illustrate the change of the wavelet. Next to the legend the RCC is shown between the wavelets.

5.2.3. Linking of the geomechanical phases with the acoustic phases

When the geomechanical data is linked to the processed data, the phases discussed in the previous section can be aligned with the stress strain diagram. The acoustic phases display similarities with the stages of the stress-strain diagram as discussed in the theory section. In Figure 5.26 a schematic overview is shown where a rock is brought under compression until rupture in the brittle field. Underneath the stress-strain curve the corresponding stages of microfracturing are shown, as was presented by Halbauer et al[20]. The boundary of phase 2 and 3 is dependant on the magnitude of change occurring inside the rock medium and the sensitivity of the coda to this. The existing and created microcracks and flaws present in the rock can be interpreted as the scatters responsible for the coda change. In this example the smooth behavior of acoustic phase 3 is shown, caused by the more gradual change of amplitudes in the wavelet.

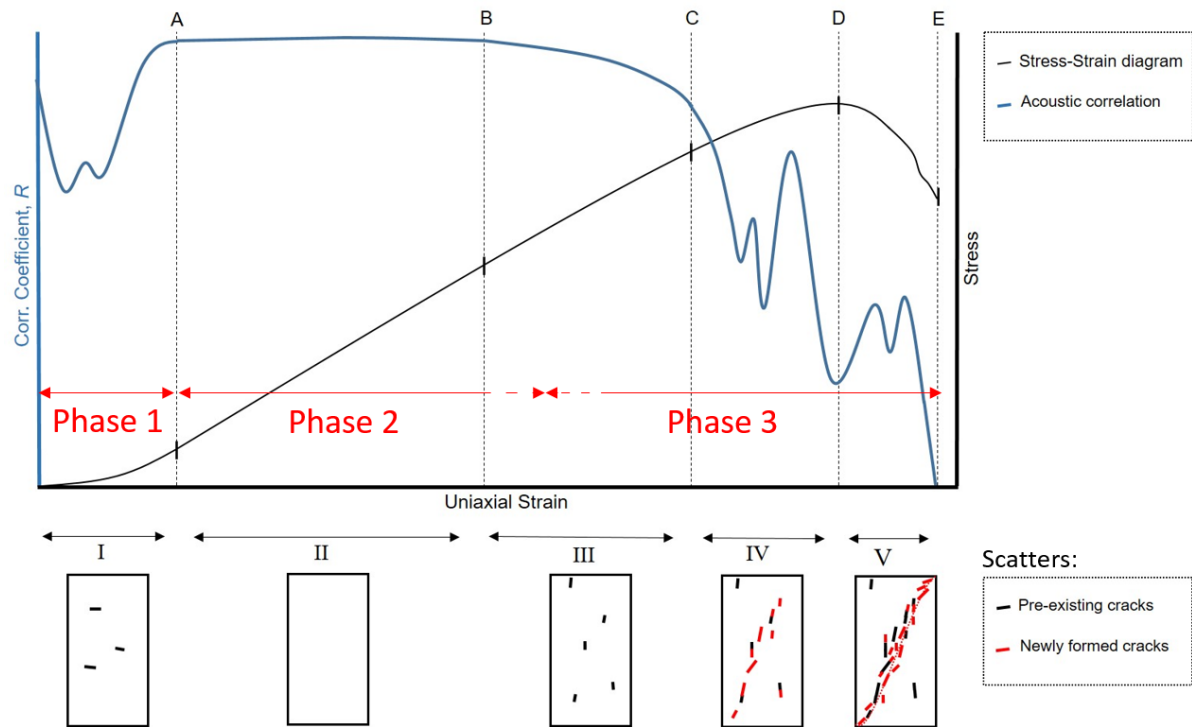


Figure 5.26: A schematic of the geomechanical stress-strain data is linked to the acoustic RCC behavior, which can be divided into three phases. For each geomechanical change a schematic is shown of the microfracture behavior in the medium (based on Halbauer)

In some cases, such as for the Indiana Limestone the coda was more sensitive to more radical wave changes in a short amount of time, which resulted in spiky behavior in the RCC. These spikes, as shown in Figure 5.10, could be linked to larger events, such as larger microcracks on the size of the grainscale as discussed in the geomechanics section. The RCC showed more erratic behavior for all tests when a higher frequency was used and thus a smaller wavelength. The onset of yielding can be detected but not the exact yieldpoint in phase 3 (yieldpoint as described in theory), because this is not a specific type of change in scatter distribution while loading continues but a linearity response of stress versus strain. This point can possibly be detected when keeping the stress constant (creep tests), to see if the fractures are still growing.

5.2.4. Frequency and microfracture size

To get an idea of the ideal frequency to identify individual events in CWI analysis there one can look at the wavelength. For seismic resolution Widess proposed a relation between the wavelength and the smallest thickness of a thinbed, $\lambda/8$ (λ is the predominant wavelength), by which the reflection can be defined [43]. For CWI analysis during brittle deformation the detection of scatterers is not the object itself but possible influence a microfracture can have on the received coda waves. Matsunami found with laboratory tests that the attenuation was the highest if the wavelength was in the same order as the dimension of the crack [26]. However, the sensitivity can be too high if the same wavelength is used as the smallest microfracture, because a smaller change of the position of the grain will result in a larger change in the wavelet. In Table 5.1

the approximate sizes of microfractures with respect to the wavelengths are shown for the different lithologies tested in this study. This is a rough indication, where the size of the microfracture was chosen in the order of the grains or crystals. The source frequency chosen to calculate the wavelength, $\lambda = v/f$. There is however a large distribution in frequencies as can be seen in Appendix C. From this Figure it can also be seen that the distribution is larger for the Fontainebleau sandstone and the granite than the Bentheimer sandstone. From Table 5.1 it can be seen that the lower ratios showed more erratic behavior, but also that from this research no specific ratio by which erratic behavior is obtained is apparent. For example FBS has a similar ratio as BNT for 1 MHz, but only the FBS showed somewhat erratic behavior in the RCC curves. More research is needed on the exact process of microfracturing size and deformation occurring in the rock and the effect it has on the RCC sensitivity.

Table 5.1: Rough estimate of the microcrack size with respect to the wavelength for the four rock types

	1 MHz	2.25 MHz
BNT	$\frac{\lambda}{17}$	$\frac{\lambda}{7}$
FBS	$\frac{\lambda}{22}$	$\frac{\lambda}{10}$
CAR	$\frac{\lambda}{4}$	
GRA	$\frac{\lambda}{20}$	$\frac{\lambda}{9}$

5.3. Comparison with AE monitoring and use in Earthquake prediction

CWI analysis could possibly be used for similar applications as Acoustic Emission (AE, or MS, Micro-seismic Activity) analysis, where both methods detect the irreversible changes due to micro-fracturing. Contradictory to the active RCC method the AE method is passive, which means it is totally dependant of the recorded acoustics by a transducer as a result of sources in the rock itself. Possible sources can be growth of micro-fractures and dislocation movements which results in a sudden loss of stored strain energy, releasing an elastic stress wave [21]. Different techniques can be used to display the acoustic emission activity, but the most common are cumulative AE count and AE rate. In Figure 5.27 an example is shown of AE activity during a test where a Bentheimer sample is brought to failure [41]. Erratic rates of AE can be seen starting directly after the crack closure area and increasing dramatically near the end of the test.

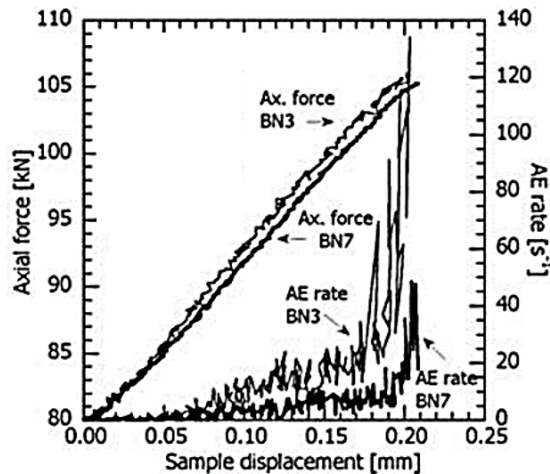


Figure 5.27: AE rates shown for two Bentheimer sampler over their stress-strain curves (displacement controlled triaxial test with $0.5 \mu\text{m}$, and a sample length of 38.1 mm and diameter of 18.4 mm) [41]

A disadvantage of Acoustic Emission monitoring is that it has a sole dependency on the generated acoustic energy received by a transducer. That energy is often several magnitudes smaller than used with active ultrasonic techniques, making the risk of attenuation or ambient noise disturbance higher [19]. The reproducibility of the AE method can be low, which can also be observed for the two similar displacement controlled tests in 5.27. The presence of AE is in itself not always a clear indicator of the state of a rock and can lead to wrong or inconsistent assumptions of the mechanical state in-situ [22]. CWI RCC may have the advantage that the calibration capabilities for testing are of a larger extent than with acoustic emission. For example, the frequency can be adjusted to a range most sensitive to the changes in the rock medium. Another advantage is that the initial energy of the pulse also depends not on the energy released in the rock but on the energy of the source transducer.

AE has proved to be a valuable tool in some cases to obtain more knowledge about the mechanical stability of stressed rocks. It is for example currently used as precursory warning tool during hydraulic fracturing to monitor the movement of nearby faults in order to prevent induced earthquakes [45]. For this application and earthquakes in general, CWI analysis can possibly be an interesting additional method to gain insight towards earthquake prediction. Main and Meredith described the event of an earthquake from a fracture mechanical point of view. In Figure 5.28 a schematic diagram is shown describing the onset of an earthquake.

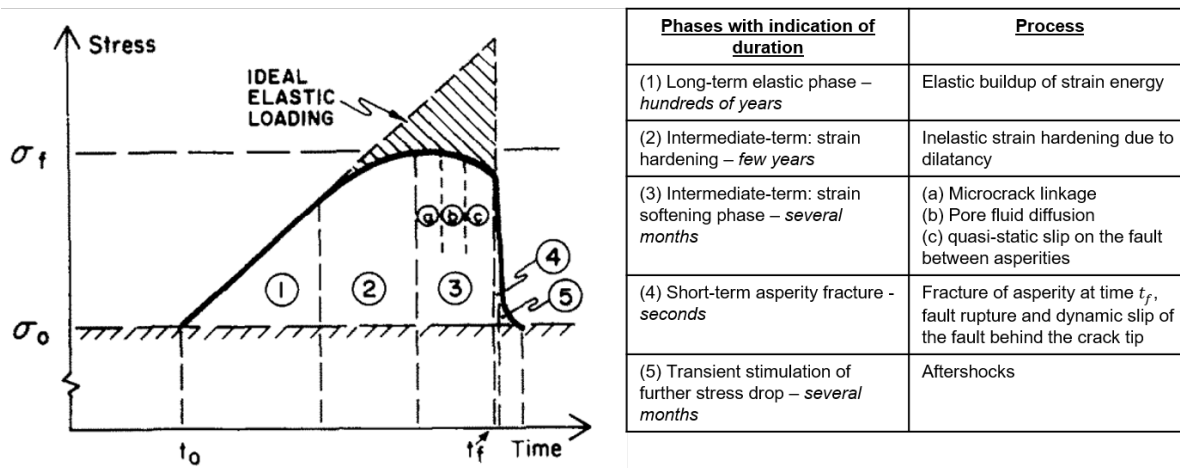


Figure 5.28: Main phases of the earthquake cycle against stress. The phases with its subdivisions are described in the table next to it. Note that the time axis is not on scale, an idea of the duration of the phase is shown in the table (Figure and modified table from Main and Meredith [25]).

The phases as described in Figure 5.28 are interesting to investigate further with CWI analysis, where the frequencies can be adjusted to the type of process taking place (with the use of upscaling). The specific type of change of the coda waves can also play a role in identifying and monitoring the type of process underway. A possible interesting fault for this method is the San Andreas Fault, a fault that is relatively easily reachable as is also visible at the surface. At present, this fault is already actively monitored with the use of special monitoring wells [8][31].

6

Conclusion

In this study Coda Wave Interferometry analysis is applied on rocks subjected to uniaxial compression to study if the failure of a rock can be monitored with the use of ultrasonic pulses as source. The general conclusions are:

- The standard time-shifted Cross Correlation with a fixed reference is sensitive to velocity changes in the medium, but when using a fixed reference it is too sensitive to coherently monitor the incremental change of scatter distributions. The dramatic change of scattering distribution is a result from microfracturing when a rock is brought to failure. A new method is proposed, the Rolling Cross Correlation, which measures the rate of change of the time-shifted Cross Correlation. This is done by not taking the fixed reference point but by taking a reference point which moves along with the measuring point by a fixed measurement interval, defined as the rolling CC lag. With this method a more usable behavior of the rock can be obtained, showing the rate of changes in the different phases of the stress-strain curve.
- The change in coda wavelets (and scatter distribution of the medium) can be subdivided into three phases. The first phase, the Rising Phase, is the phase where fracture closure occurs, resulting in increased coupling and changes in scatter distribution. In the second phase, the Plateau, there is little change in coda. This is the purely elastic phase where the lack of microfracturing is dominant and thus change in scatter distribution is low. In the third phase, the Falling Phase, there is an overall decrease in the cross-correlation number. In this phase the dominant mechanism is microfracturing, which results in a change of scatter distribution. The detection of initial fracturing can be seen as a precursor to yielding and thus failure. The subdivision of dominantly stable or unstable fractures (yield point) can not be made with the current method, because this transition is purely a linearity response of the stress-strain relationship, which is not detectable with CWI.
- The RCC proved sensitive to the frequency used and the size of the changing events. The method could monitor the larger individual activated flaws/fractures with respect to the wavelength. Especially the third phase for the Fontainebleau sandstone and the Indiana Limestone tests showed a high correlation between rapid increase of strain and dips in the RCC. When using a higher source frequency this behavior of local dips was enhanced for the Bentheimer Sandstone, the Fontainebleau Sandstone and the Benin Granite tests.
- In the data processing the RCC curves are dependant in the total measurement numbers taken, correlation lag and the size and position of the correlation window. When using higher correlation lag the more general trends will become visible, while local events are better visible with low rolling correlation lag. The correlation window to capture the behavior can be best picked excluding the coherent arrivals at the start of the wavelet. These are of higher amplitude and thus of large effect on the correlation number. The amount of measurement points needed depends on the amount and magnitude of change. With sixty measurements the general trends were visible, while individual events became better visible when more than 150 measurements were taken for the laboratory UCS tests done in this study.

- For future work it is recommended to study the change in frequency while deforming a rock. This and by looking at the type of change in the coda wavelet can possibly aid in the identification of the specific type of change taking place in the medium. Additionally, microscopic, x-ray and numerical studies can enhance the correlation between change in medium and the change in coda. Upscaling and different geomechanical tests (for example triaxial testing and tests with saturated rocks) are recommended to research for in-situ applicability.

Acknowledgements

First of all I would like to thank my two supervisors. Auke for his guidance and making it possible to do this research combining different aspects of geoscience. My special thanks to Reuben as daily supervisor for always being available for guidance and for all the interesting discussions about the topic. I would like to thank Lisanne Douma and Richard Bakker for their support and knowledge of lab testing and geomechanics. Furthermore I'd like to thank Guy Drijkoningen and Pacelli Zitha for taking place in my committee. Maaïke van Tooren is thanked for her help with the microscope and refreshing my knowledge of minerals. I would like to thank the Geoscience and Engineering lab technicians at TU Delft, especially Karel Heller. He was always available to help with the acoustic setup and he automated the acoustic data acquisition, which made it possible to do the various tests. Last, I would like to thank my parents, my sister and Emily for their continuous support in many ways not only during my thesis but also during the various phases of study.

Bibliography

- [1] A. Barnhoorn, J. Verheij, M. Frehner, A. Zhubayev, and M. Houben. Transition from elastic to inelastic deformation identified by a change in trend of seismic attenuation, not seismic velocity—a laboratory study. In *EGU General Assembly Conference Abstracts*, volume 18, page 5937, 2016.
- [2] P. Baud, A. Schubnel, and T. Wong. Dilatancy, compaction, and failure mode in solnhofen limestone. *Journal of Geophysical Research: Solid Earth*, 105(B8):19289–19303, 2000.
- [3] Z.T. Bieniawski. Mechanism of brittle fracture of rock: part i—theory of the fracture process. In *International Journal of Rock Mechanics and Mining Sciences & Geomechanics Abstracts*, volume 4, pages 395IN11405–404IN12406. Elsevier, 1967.
- [4] A. Bodare. Non destructive test methods of stone and rock. Division of Soil and Rock Mechanics, Department of Civil and Environmental Engineering; Royal Institute of Technology: Stockholm, 1996.
- [5] A. Bogusz and M. Bukowska. Stress-strain characteristics as a source of information on the destruction of rocks under the influence of load. *Journal of Sustainable Mining*, 14(1):46–54, 2015.
- [6] T. Bourbie and B. Zinszner. Hydraulic and acoustic properties as a function of porosity in fontainebleau sandstone. *Journal of Geophysical Research: Solid Earth*, 90(B13):11524–11532, 1985.
- [7] W.F. Brace. *Brittle fracture of rocks*. Massachusetts Institute of Technology, Industrial Liaison Program, 1963.
- [8] F. Brenguier, M. Campillo, C. Hadziioannou, N.M. Shapiro, R.M. Nadeau, and Eric Larose. Postseismic relaxation along the san andreas fault at parkfield from continuous seismological observations. *science*, 321(5895):1478–1481, 2008.
- [9] P.L. Churcher, P.R. French, J.C. Shaw, L.L. Schramm, et al. Rock properties of berea sandstone, baker dolomite, and indiana limestone. In *SPE International Symposium on Oilfield Chemistry*. Society of Petroleum Engineers, 1991.
- [10] M.R. Cooper, J. Evans, S.S. Flint, A.J.C. Hogg, and R.H. Hunter. Quantification of detrital, authigenic and porosity components of the fontainebleau sandstone: A comparison of conventional optical and combined scanning electron microscope-based methods of modal analyses. *Quartz cementation in sandstones*, pages 89–101, 2009.
- [11] G. Dresen, S. Stanchits, and E. Rybacki. Borehole breakout evolution through acoustic emission location analysis. *International Journal of Rock Mechanics and Mining Sciences*, 47(3):426–435, 2010.
- [12] R.J. Dunham. Classification of carbonate rocks according to depositional textures. 1962.
- [13] E. Eberhardt, D. Stead, and B. Stimpson. Quantifying progressive pre-peak brittle fracture damage in rock during uniaxial compression. *International Journal of Rock Mechanics and Mining Sciences*, 36(3): 361–380, 1999.
- [14] G.M. Elliott and E.T. Brown. Further development of a plasticity approach to yield in porous rock. In *International Journal of Rock Mechanics and Mining Sciences & Geomechanics Abstracts*, volume 23, pages 151–156. Elsevier, 1986.
- [15] J. Fortin, S. Stanchits, G. Dresen, and Y. Guéguen. Acoustic emission and velocities associated with the formation of compaction bands in sandstone. *Journal of Geophysical Research: Solid Earth*, 111(B10), 2006.
- [16] A. Grêt. *Time-Lapse Monitoring with Coda Wave Interferometry*. PhD thesis, Colorado School of Mines, 2004.

- [17] A. Grêt, R. Snieder, and J. Scales. Time-lapse monitoring of rock properties with coda wave interferometry. *Journal of Geophysical Research: Solid Earth*, 111(B3), 2006.
- [18] A.A. Griffith. The phenomena of rupture and flow in solids. *Philosophical transactions of the royal society of london. Series A, containing papers of a mathematical or physical character*, 221:163–198, 1921.
- [19] C.U. Grosse and M. Ohtsu. *Acoustic emission testing*. Springer Science & Business Media, 2008.
- [20] D.K. Hallbauer, H.N.G.W. Wagner, and N.G.W. Cook. Some observations concerning the microscopic and mechanical behaviour of quartzite specimens in stiff, triaxial compression tests. In *International Journal of Rock Mechanics and Mining Sciences & Geomechanics Abstracts*, volume 10, pages 713–726. Elsevier, 1973.
- [21] H.R. Hardy Jr. *Acoustic emission/microseismic activity: volume 1: principles, techniques and geotechnical applications*, volume 1. CRC Press, 2005.
- [22] D.J. Holcomb. General theory of the kaiser effect. In *International Journal of Rock Mechanics and Mining Sciences & Geomechanics Abstracts*, volume 30, pages 929–935. Elsevier, 1993.
- [23] J.C. Jaeger, N.G.W. Cook, and R. Zimmerman. *Fundamentals of rock mechanics*. John Wiley & Sons, 2009.
- [24] D.A. Lockner, D.E. Moore, Z.E. Reches, et al. Microcrack interaction leading to shear fracture. In *The 33th US Symposium on Rock Mechanics (USRMS)*. American Rock Mechanics Association, 1992.
- [25] I.G. Main and P.G. Meredith. Classification of earthquake precursors from a fracture mechanics model. *Tectonophysics*, 167(2-4):273–283, 1989.
- [26] K. Matsunami. Laboratory measurements of spatial fluctuation and attenuation of elastic waves by scattering due to random heterogeneities. *pure and applied geophysics*, 132(1):197–220, 1990.
- [27] G. Mavko, E. Kjartansson, and K. Winkler. Seismic wave attenuation in rocks. *Reviews of Geophysics*, 17(6):1155–1164, 1979.
- [28] G. Mavko, T. Mukerji, and J. Dvorkin. *The rock physics handbook: Tools for seismic analysis of porous media*. Cambridge university press, 2009.
- [29] K. Mogi. *Experimental rock mechanics*, volume 3. CRC Press, 2007.
- [30] L. Nasdala, M. Wenzel, M. Andrut, R. Wirth, and P. Blaum. The nature of radiohaloes in biotite: Experimental studies and modeling. *American Mineralogist*, 86(4):498–512, 2001.
- [31] F. Niu, Paul G. Silver, T.M. Daley, X. Cheng, and E.L. Majer. Preseismic velocity changes observed from active source monitoring at the parkfield safod drill site. *Nature*, 454(7201):204–208, 2008.
- [32] M.S. Paterson and T. Wong. *Experimental rock deformation-the brittle field*. Springer Science & Business Media, 2005.
- [33] A.E. Peksa, K.A.A. Wolf, and P.L.J. Zitha. Bentheimer sandstone revisited for experimental purposes. *Marine and Petroleum Geology*, 67:701–719, 2015.
- [34] S. Peng and A.M. Johnson. Crack growth and faulting in cylindrical specimens of chelmsford granite. In *International Journal of Rock Mechanics and Mining Sciences & Geomechanics Abstracts*, volume 9, pages 37IN543IN761IN1575–42IN660IN1474IN1886. Elsevier, 1972.
- [35] H. Sato, M.C. Fehler, and T. Maeda. *Seismic wave propagation and scattering in the heterogeneous earth*, volume 484. Springer, 2012.
- [36] S.F. Selleck, E.N. Landis, M.L. Peterson, S.P. Shah, and J.D. Achenbach. Ultrasonic investigation of concrete with distributed damage. *Materials Journal*, 95(1):27–36, 1998.
- [37] C. Sens-Schönfelder and U. Wegler. Passive image interferometry and seasonal variations of seismic velocities at merapi volcano, indonesia. *Geophysical research letters*, 33(21), 2006.
- [38] N.M. Smith. Sedimentology of the salem limestone in indiana. 66(2):168–179, 1966.

-
- [39] R. Snieder. The theory of coda wave interferometry. *Pure and Applied Geophysics*, 163(2-3):455–473, 2006.
- [40] R. Snieder, A. Grêt, H. Douma, and J. Scales. Coda wave interferometry for estimating nonlinear behavior in seismic velocity. *Science*, 295(5563):2253–2255, 2002.
- [41] V. Vajdova and T. Wong. Incremental propagation of discrete compaction bands: Acoustic emission and microstructural observations on circumferentially notched samples of bentheim. *Geophysical Research Letters*, 30(14), 2003.
- [42] J. Verheij. Seismic attenuation analyses of fracturing in reservoir rocks. Master's thesis, Delft University of Technology, 2015.
- [43] M.B. Widess. How thin is a thin bed? *Geophysics*, 38(6):1176–1180, 1973.
- [44] K.W. Winkler. Frequency dependent ultrasonic properties of high-porosity sandstones. *Journal of Geophysical Research: Solid Earth*, 88(B11):9493–9499, 1983.
- [45] Witteveen+Bos, ARCADIS, and FUGRO. *Aanvullend onderzoek naar mogelijke risico's en gevolgen van de opsporing en winning van schalie- en steenkoolgas in Nederland Eindrapport onderzoeksvragen A en B*. Ministerie van Economische Zaken Directie Energiemarkt, 2013.
- [46] S. Yang, Y. Huang, W. Tian, and J. Zhu. An experimental investigation on strength, deformation and crack evolution behavior of sandstone containing two oval flaws under uniaxial compression. *Engineering Geology*, 217:35–48, 2017.

Appendix A

Table A.1: Laboratory test settings and sample properties

	Dataset	Length [mm]	Diameter [mm]	Displacement Rates [mm/s]	UCS [MPa]	Young's modulus [GPa]	Position of receiver(s)
Bentheimer Sandstone	BNT_1	59.92	39.73	0.0005	46.1	10.4	1 axial
	BNT_2	75.01	39.70	0.0005	42.0	10.2	1 axial, 2 radial
	BNT_3	75.00	30.00	0.0005	33.2	10.5	1 axial, 2 radial
Fontainebleau Sandstone	FBS_1	70.68	29.79	0.0002	156.5	30.4	1 axial, 2 radial
	FBS_2	70.02	29.78	0.0002	153.1	20.5	1 axial, 2 radial
	FBS_3	70.73	29.78	0.0002	129.5	29.4	1 axial, 2 radial
	FBS_4HF	75.34	29.82	0.0002	146.1	27.5	1 radial
Indiana Limestone	CAR_1	74.69	29.72	0.00005	29.4	15.4	1 axial, 2 radial
Benin Granite	GRA_1	70.90	28.74	0.0002	-	42.9	1 axial, 2 radial
	GRA_3HF	80.30	29.77	0.0001	207.6	37.5	1 axial

Appendix B

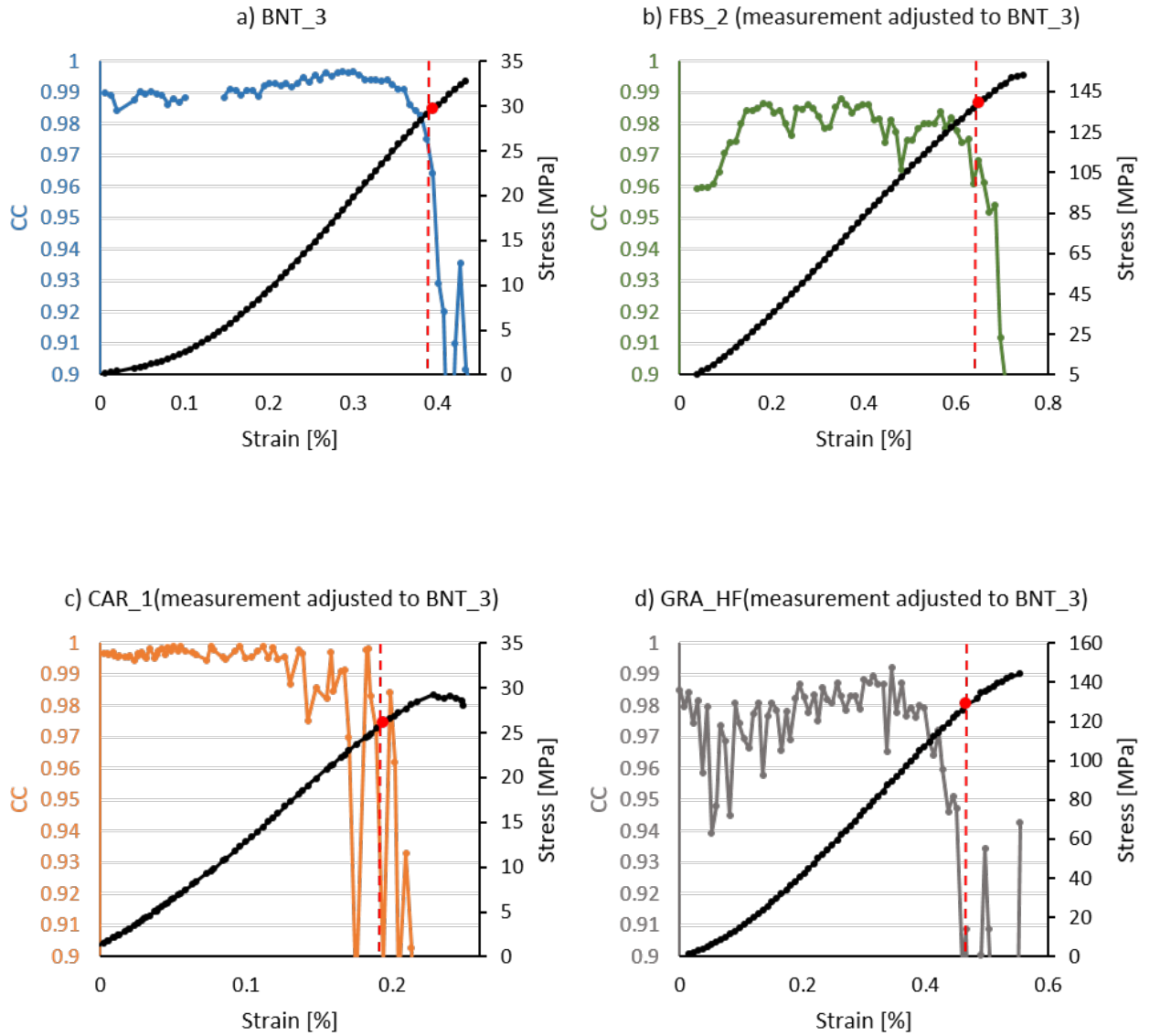


Figure B.1: Measurement adjusted curves to the BNT_3 test to obtain an equal amount of measurement points taken over the stress-strain curvature. The yield points are hand-picked from the stress-strain curve and indicated with a red marker and dashed line for each rock. For all RCC curves a correlation lag of 1 measurement was used.

Appendix C

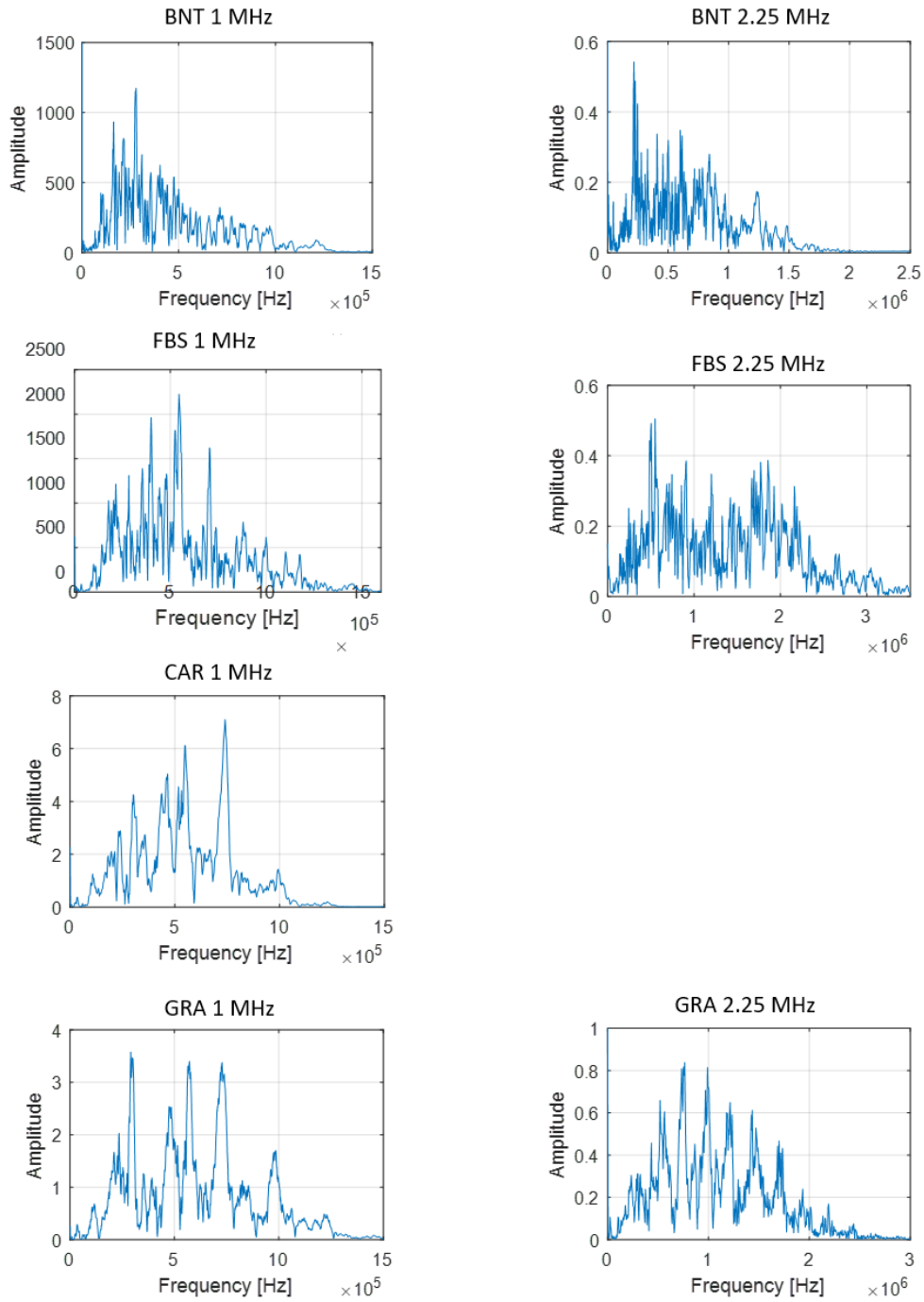


Figure C.1: Frequency domain plots of the different lithologies for the total wavelet. Wavelets were in the elastic area of stress-strain curve and plateau area of RCC curves. Figures give an idea of the frequency distribution as it is received by the transducer.